Eidgenössische Technische Hochschule Zürich

Ecole polytechnique fédérale de Zurich
Politecnico federale di Zurigo
Swiss Federal Institute of Technology Zurich

Is the transonic flow around a cylinder always periodic?

Nicola Botta

Research Report No. 92-15
December 1992

Seminar für Angewandte Mathematik
Eidgenössische Technische Hochschule
CH-8092 Zürich
Switzerland

Is the transonic flow around a cylinder always periodic ?

Nicola Botta
Seminar für Angewandte Mathematik
Eidgenössische Technische Hochschule
CH-8092 Zürich
Switzerland

Research Report No. 92-15 December 1992

Abstract

The inviscid transonic flow about a circular cylinder is investigated at large times. For this scope the Euler equations are integrated numerically, according to a time dependent technique. The integration is based on an high resolution finite volume upwind method.
Transitions to qualitatively different families of solutions have been observed by increasing the value of the free stream Mach number from 0.5 up to 1. In particular the breakdown of the periodic solution into an irregularly oscillating flow was noticed.
Goal of this work is the description of these transitions and their interpretation on the basis of the physics of inviscid flow.

Keywords: unsteady transonic flow, circular cylinder, Euler equations

Subject Classification: 35L65, 76M10

Eidgenössische
Technische Hochschule
Zürich

Seminar für
Angewandte
Mathematik
SAM

Is the transonic flow around a cylinder always periodic?

Nicola Botta

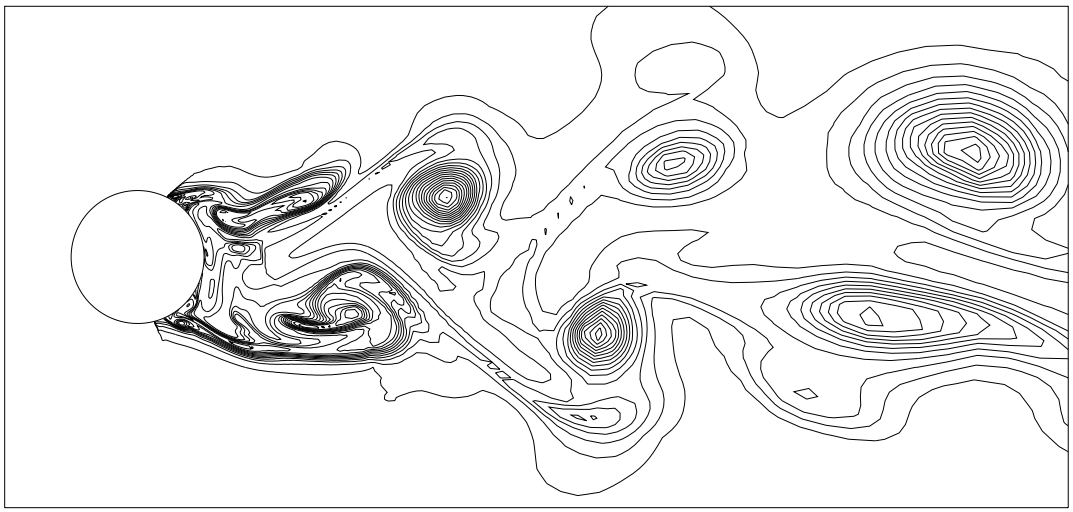

Research Report No. 92-15
December 1992

Seminar für Angewandte Mathematik
Eidgenössische Technische Hochschule
CH-8092 Zürich
Switzerland

Is the transonic flow around a cylinder always periodic ?

Nicola Botta
Seminar für Angewandte Mathematik
Eidgenössische Technische Hochschule
CH-8092 Zürich
Switzerland

Research Report No. 92-15 December 1992

Abstract

The inviscid transonic flow about a circular cylinder is investigated at large times. For this scope the Euler equations are integrated numerically, according to a time dependent technique. The integration is based on an high resolution finite volume upwind method.
Transitions to qualitatively different families of solutions have been observed by increasing the value of the free stream Mach number from 0.5 up to 1. In particular the breakdown of the periodic solution into an irregularly oscillating flow was noticed.
Goal of this work is the description of these transitions and their interpretation on the basis of the physics of inviscid flow.

Keywords: unsteady transonic flow, circular cylinder, Euler equations

Subject Classification: 35L65, 76M10

1. The physical problem

In the last decade a significant effort has been devoted to the numerical prediction of two-dimensional compressible inviscid flows through the numerical integration of the Euler equations. In particular the transonic flow about a circular cylinder has been the subject of many investigations ([1]-[4],[12],[13]). Let us consider, for given initial and boundary conditions, a steady state solution of this problem. If this exists, it depends on only one parameter. Let this parameter be the free stream Mach number (M_∞). Consider the two sketches of fig.2:

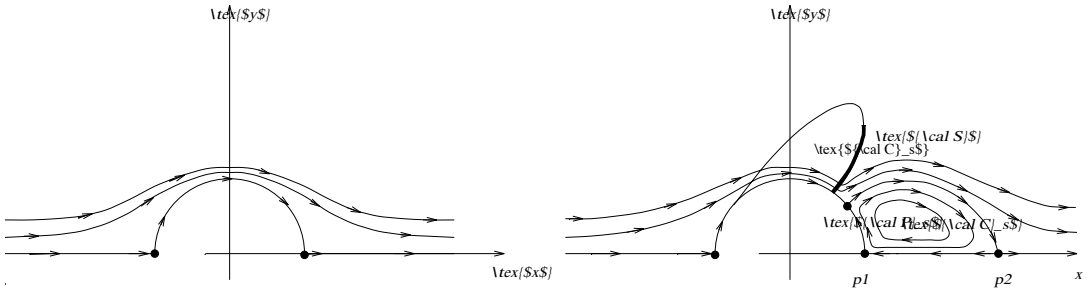

Figure 2: *subcritical (left) and transonic flow (right); steady state solution*

on the left side a subcritical case is drawn. All over the flow field the Mach number is less than one. The flow is isentropic and therefore reversible (since the Euler equations do not allow thermal exchange). Thus, provided that the boundary conditions are homentropic and homenergetic (we do not consider here cases where the cylinder is embedded in a wake), the flow is symmetric with respect to the x- as well as with respect to the y-axis. This is the flow that can be observed (computed) for $M_\infty < M_{\infty cr} \approx .4$. On the right side of fig.2 a steady state solution for the transonic case ($M_{\infty cr} < M_\infty < 1$) has been depicted. A supersonic region $\mathcal{C}_s$ appears around the maximum thickness point of the cylinder. On the lee side of this region the flow returns to the subsonic regime through a radial shock wave $\mathcal{S}$. This causes total pressure losses that hinder the flow wetting the cylinder to reach the rear stagnation point $\mathcal{P}_1$ on the symmetry axis. The flow separates at the point $\mathcal{P}_s$. This separated flow is highly rotational and its vorticity is roughly proportional to the inverse of the radial extension of the shock. To see that this is true we recall Crocco's theorem for the inviscid steady case:

$$T\nabla s = -\mathbf{v} \times (\nabla \times \mathbf{v}) + \nabla h_0 \tag{1}$$

Here T is the (absolute) temperature of the flow, s the entropy, $\mathbf{v}$ the velocity vector and h_0 the total enthalpy. For the two-dimensional case in a cylindrical frame of reference z, ρ, θ with unit vectors $\mathbf{a}$, $\mathbf{b}$ and $\mathbf{c}$ and $\mathbf{v} = v_\rho \mathbf{b} + v_\theta \mathbf{c}$ lying in the plane normal to $\mathbf{a}$ (1) gives:

$$\omega = -\frac{T}{v_\theta}\frac{\partial s}{\partial \rho} \;=\; -K\frac{T}{v_\theta}\frac{\Delta s_{sh}}{\Delta \rho_{sh}}, \quad \omega \mathbf{a} = \nabla \times \mathbf{v} \tag{2}$$

and the vorticity is seen to be directly proportional to the entropy jumps across the shock Δs_{sh} and inversely proportional to the radial extension of the shock $\Delta \rho_{sh}$. The separeted flow streams along a circulating bubble $\mathcal{C}_c$ toward the rear stagnation point $\mathcal{P}_2$ and conveys the entropy gradients into a wake parallel to the x-axis. Thus the wake down the cylinder is a vortex layer whose thickness (and intensity) depend on the radial extension of the shock. In this layer $\omega(y) = -\omega(-y)$ since v_θ is an odd function of y and Δs_{sh} must be non negative in order to satisfy the second principle of thermodynamics. We just remind that the limit case of an infinitesimal vortex sheet as solution of the incompressible inviscid equations is unstable ([5] pagg. 511-517). Inside $\mathcal{C}_c$ the streamlines are closed paths. What are the values of the entropy which are conveyed along these orbits? Are these values a rest of the history of the flow? (But in this case how can we refer to this solution as to *the* steady state solution?).

In a GAMM workshop [3] two test cases focused on the transonic cylinder problem were proposed to the attention of the contributors: the ones for values of the free stream Mach number of 0.5 and 0.6. The results of these computations were some way disturbing: numerical methods designed to compute a steady state solution gave scattered results concerning the size of the

circulating bubble or even did not converge. On the other hand methods based on a true time integration of the full Euler equations showed very similar unsteady solutions for both test cases (contributions C17, C18 and C20 in [3]). A deeper insight in the understanding of the physics of these flows was given by Pandolfi and Larocca [4]. They used a second order accurate finite difference method based on an upwind hybrid formulation of the Euler equations and a time dependent technique. For both cases they found that the symmetrical solution with a radial shock followed by an inviscid separation and a circulating bubble was unsteady. Periodical oscillations of the shock position were coupled with a cyclic variation of the size of the circulating bubble. For the $M_\infty = 0.6$ case they also observed the recurrent detachment of the circulating bubble and its convection in the wake. Thus they could explain the disturbing results found in [3]. Moreover they removed the upsetting question about the meaning of closed paths in the steady state: actually they did not find any stationary solution!
In addition they observed that, for both test cases, this periodical symmetrical solution was unstable in the sense that asymmetries of the round of error (due to a different sequence of operations performed on symmetrical points to update symmetrical initial data) led to an asymmetrical periodic flow. Here the radial shocks on the sides of the circular cylinder oscillate alternately shedding eddies into a wake whose structure is very similar to that of the von Karman vortex street observed in the incompressible viscous case (see picture on the cover where entropy contour lines are traced). They also showed that this phenomena is consistent with the physics of a compressible inviscid flow and that the numerical viscosity due to the discretization does not affect qualitatively the results. In particular, for the $M_\infty = 0.6$ case, a more complex pattern of shock waves was seen to appear in the flow. Beside the primary shocks a third intermittent one was observed, due to the strong rotation induced by the curvature of a primary one (fig.12 of [4] and figg. 16 and 28 here). In spite of its complexity the flow was perfectly periodic. These results (for $M_\infty = 0.5$ and $M_\infty = 0.6$) have been recently confirmed by Di Mascio [13] as well as by our computations.

We have used an high resolution finite volume upwind method to compute numerically the flow about the circular cylinder for values of M_∞ between 0.5 and 1. At large times the flow reaches, for M_∞ in the low transonic regime, a limit cycle. This is stable and does not depend sensitively on the initial condition and on the discretization. However, for higher values of M_∞ the flow exhibits a stranger behaviour: at $M_\infty = 0.75$ the main bulk of the flow still swings but delays in the onset of successive phases of the oscillation prevent the achievement of a limit cycle. Instead "islands" of regularity seems to characterize the (aperiodic?) orbit of the flow. At $M_\infty = 0.8$ the flow returns to a perfectly periodic oscillation but a further increase of this parameter leads to a renewed break down of regularity. Finally, for values of the $M_\infty \approx 1$ the flow seems to return to a steady solution. In the following section we outline the numerical method and the initial and boundary conditions. In the third we present the numerical results and interpret the transitions described above on the basis of the physics of an inviscid flow. For the $M_\infty = 0.85$ case we discuss the behaviour of the flow after the breakdown of the symmetric solution and at some later time. We try to explain this behaviour with a numerical conjecture. Finally we figure out some conclusions.

2. The numerical method.

Finite volume method, computation of the fluxes.
Let $\mathcal{C} \subset \mathbb{R}^2$ be a region of the physical space around the circular cylinder and $\mathcal{C}_{i,j}$ ($i = 1, \ldots, nc1$ and $j = 1, \ldots, nc2$) the rectangular cells of a structured discretization of $\mathcal{C}$. Let also the boundary of $\mathcal{C}_{i,j}$ consist of the four cell interfaces $\partial\mathcal{C}1_{i,j}$, $\partial\mathcal{C}1_{i+1,j}$, $\partial\mathcal{C}2_{i,j}$ and $\partial\mathcal{C}2_{i,j+1}$ normal to the first (index 1) and to the second (index 2) coordinate lines of a curvilinear frame of reference. Let $\mathbf{n}$ be the unit vector normal to the cell interfaces and oriented in the positive direction of the coordinate lines and n_x, n_y the components of $\mathbf{n}$ in a fixed Cartesian frame of reference x, y (fig.3).

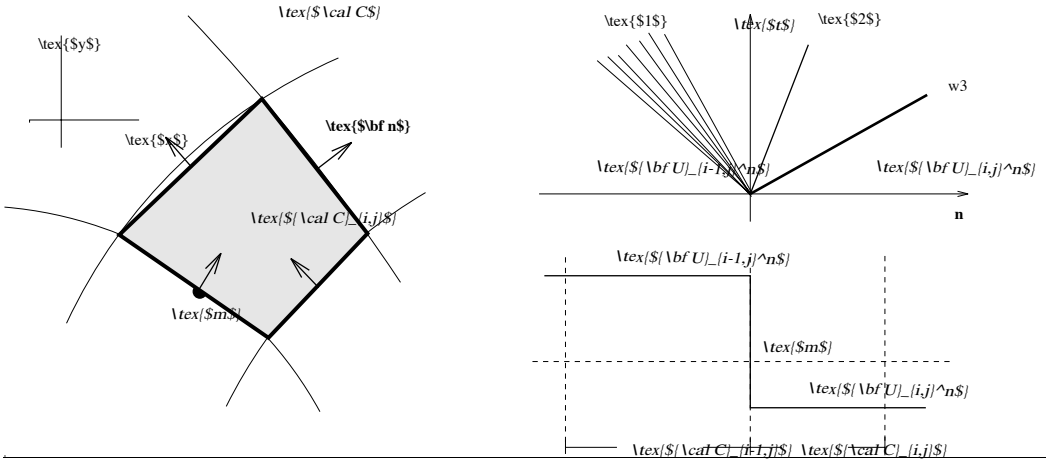

Figure 3: *Domain discretization (left) and 1D Riemann problem (right)*

The Euler equations can be written as conservation laws for the $\mathcal{C}_{i,j}$ control volume:

$$\frac{\partial}{\partial t}\int_{\mathcal{C}_{i,j}} \mathbf{u}(\mathbf{x},t)\,ds = -\int_{\partial\mathcal{C}1_{i+1,j}} \mathbf{f}(\mathbf{u}(\mathbf{x},t),\mathbf{n}(\mathbf{x}))\,dl + \int_{\partial\mathcal{C}1_{i,j}} \mathbf{f}(\mathbf{u}(\mathbf{x},t),\mathbf{n}(\mathbf{x}))\,dl + \\ - \int_{\partial\mathcal{C}2_{i,j+1}} \mathbf{f}(\mathbf{u}(\mathbf{x},t),\mathbf{n}(\mathbf{x}))\,dl + \int_{\partial\mathcal{C}2_{i,j}} \mathbf{f}(\mathbf{u}(\mathbf{x},t),\mathbf{n}(\mathbf{x}))\,dl \tag{3}$$

with

$$\mathbf{u} = \begin{pmatrix} \rho \\ \rho\mathbf{v} \\ \rho e \end{pmatrix} \qquad \mathbf{f} = \begin{pmatrix} \rho(\mathbf{v}\cdot\mathbf{n}) \\ p\mathbf{n} + \rho\mathbf{v}(\mathbf{v}\cdot\mathbf{n}) \\ (\rho e + p)(\mathbf{v}\cdot\mathbf{n}) \end{pmatrix} \qquad p = (\gamma-1)(\rho e - \frac{1}{2}\rho\mathbf{v}\cdot\mathbf{v})$$

where ρ is the density, $\mathbf{v}$ the velocity vector, p the pressure and e the total specific energy of the flow (the heat coefficients ratio γ is set equal to 1.4). Let us introduce the cell averages $\mathbf{U}^n_{i,j}$ and the flux functions $\mathbf{f1}_{i,j}$, $\mathbf{f1}_{i+1,j}$, $\mathbf{f2}_{i,j}$ and $\mathbf{f2}_{i,j+1}$ as follows:

$$\mathbf{U}^n_{i,j} = \frac{1}{S_{i,j}}\int_{\mathcal{C}_{i,j}} \mathbf{u}(\mathbf{x},t)\,ds \qquad\qquad S_{i,j} = \int_{\mathcal{C}_{i,j}} ds \tag{4}$$

$$\mathbf{f1}_{i,j} = \frac{1}{\Delta t_n}\frac{1}{h1_{i,j}}\int_{t_n}^{t_{n+1}}\int_{\partial\mathcal{C}1_{i,j}} \mathbf{f}(\mathbf{u}(\mathbf{x},t),\mathbf{n}(\mathbf{x}))\,dl\,dt \qquad \Delta t_n = \int_{t_n}^{t_{n+1}} dt \qquad h1_{i,j} = \int_{\partial\mathcal{C}1_{i,j}} dl \tag{5}$$

and similar expressions for $\mathbf{f1}_{i+1,j}$, $\mathbf{f2}_{i,j}$ and $\mathbf{f2}_{i,j+1}$. Integrating (3) between t_n and t_{n+1} and substituting (4) and (5) gives:

$$\mathbf{U}^{n+1}_{i,j} = \mathbf{U}^n_{i,j} - \frac{\Delta t_n}{S_{i,j}}\left[h1_{i+1,j}\mathbf{f1}_{i+1,j} - h1_{i,j}\mathbf{f1}_{i,j}\right] - \frac{\Delta t_n}{S_{i,j}}\left[h2_{i,j+1}\mathbf{f2}_{i,j+1} - h2_{i,j}\mathbf{f2}_{i,j}\right] \tag{6}$$

Let now $\mathbf{F1}_{i,j}$ be an approximation to the flux function $\mathbf{f1}_{i,j}$.

Thus for instance

$$\mathbf{F1}_{i,j} = \mathbf{f}(\mathbf{u}(\mathbf{x}_p, t_n), \mathbf{n}(\mathbf{x}_p)) \tag{7}$$

$$\mathbf{F1}_{i,j} = \mathbf{f}(\mathbf{u}(\mathbf{x}_p, t_n + \Delta t_n/2), \mathbf{n}(\mathbf{x}_p)) \tag{8}$$

are a first order and a second order approximation to $\mathbf{f1}_{i,j}$ (if p is the middle point of the $\partial\mathcal{C}1_{i,j}$ cell interface as in figure 3). The following of this section deals with the computation of $\mathbf{F1}_{i,j}$.

For this let us consider a one dimensional Riemann problem (R.p.) in the direction $\mathbf{n}(\mathbf{x}_p)$ and with initial data $\mathbf{U}^n_{i-1,j}$ and $\mathbf{U}^n_{i,j}$ on the left and right sides of $\partial\mathcal{C}1_{i,j}$ (fig.3 right bottom). Then the (self similar) solution of this R.p. for $t \geq t_n$ provides the intermediate state $\mathbf{u}(\mathbf{x}_p, t_n)$ for the right hand side of (7). Following the ideas proposed in [7] we solve this R.p. approximatively by regarding the acoustic waves as if they were isentropic. Although the non linearity of the problem is retained and the (straightforward) solution of a (non linear) system of equations allows the computation of the fields between the np waves rising from the breakdown of the discontinuity $\mathbf{U}^n_{i,j} - \mathbf{U}^n_{i-1,j}$ at the $\partial\mathcal{C}1_{i,j}$ cell interface (fig.3 right top). Thus for each wave the jumps $\mathbf{\Delta U1}_{p,i,j}$ of the conservative variables across the wave (index p) as well as the jumps of the flux function $\mathbf{\Delta F1}_{p,i,j}$ can be computed. Both $\mathbf{\Delta U1}_{p,i,j}$ and $\mathbf{\Delta F1}_{p,i,j}$ are vectors in $\mathbb{R}^4$. Let us introduce a diagonal matrix $\mathbf{\Lambda 1}_{p,i,j}$ so that

$$\mathbf{\Delta F1}_{p,i,j} = \mathbf{\Lambda 1}_{p,i,j}\mathbf{\Delta U1}_{p,i,j} \tag{9}$$

holds. Notice that, if the wave p is a discontinuity traveling at speed $\Lambda 1_{p,i,j}$ then we should have $(\mathbf{\Lambda 1}_{p,i,j})_{kk} = \Lambda 1_{p,i,j}$ for all k because of the Rankine-Hugoniot relationships. In general we just have $(\mathbf{\Lambda 1}_{p,i,j})_{kk} \approx \Lambda 1_{p,i,j}$ since the R.p. has been solved in the isentropic approximation. Let also $\mathbf{\Lambda 1}^+_{p,i,j} = 0.5(\mathbf{\Lambda 1}_{p,i,j} + |\mathbf{\Lambda 1}_{p,i,j}|)$ so that only the waves with positive speeds are accounted for. Then with (9) and (7) we have

$$\mathbf{F1}_{i,j} = \mathbf{f}(\mathbf{u}(\mathbf{x}_p, t_n), \mathbf{n}(\mathbf{x}_p)) = \mathbf{f}(\mathbf{U}^n_{i,j}, \mathbf{n}(\mathbf{x}_p)) - \sum_{p=1}^{np} \mathbf{\Lambda 1}^+_{p,i,j}\mathbf{\Delta U1}_{p,i,j} \tag{10}$$

and we have written an approximate version of Godunov's method. To achieve an higher approximation to $\mathbf{f1}_{i,j}$ we follow the wave propagation approach described in [8]. Consider equation (10). One can think of $\mathbf{F1}_{i,j}$ as consisting of the flux function on the right side of the $\partial\mathcal{C}1_{i,j}$ cell interface $\mathbf{f}(\mathbf{U}_{i,j}, \mathbf{n}(\mathbf{x}_p))$ and of corrections due to the waves entering the $\mathcal{C}_{i,j}$ cell at time t_n. Further one can think of each wave (form) as a single discontinuity $\mathbf{\Delta U1}_{p,i,j}$ traveling at speed $\mathbf{\Lambda 1}_{p,i,j}$ and changing the flux function at the interface for $\mathbf{\Lambda 1}_{p,i,j}\mathbf{\Delta U1}_{p,i,j}$ (fig.4 left). Let us now modify the wave (form) by introducing a slope $\mathbf{\Sigma 1}_{p,i,j}$ over the length $l1_{i-1,j}$ of the $\mathcal{C}_{i-1,j}$ cell and in the direction of $\mathbf{n}(\mathbf{x}_p)$ (fig.4 right top). Let us now propagate this modified wave (form) for the time interval $\Delta t_n/2$ with the same speed as the original one. With $\mathbf{I}$ the identity matrix in $\mathbb{R}^4$ the flux correction due to the modified wave is (fig.4b bottom)

$$-\mathbf{\Lambda 1}_{p,i,j}\mathbf{y} = -\mathbf{\Lambda 1}_{p,i,j}\mathbf{\Delta U1}_{p,i,j} + \frac{1}{2}\mathbf{\Lambda 1}_{p,i,j}(\mathbf{I}\,l1_{i-1,j} - \mathbf{\Lambda 1}_{p,i,j}\Delta t_n)\mathbf{\Sigma 1}_{p,i-1,j} \tag{11}$$

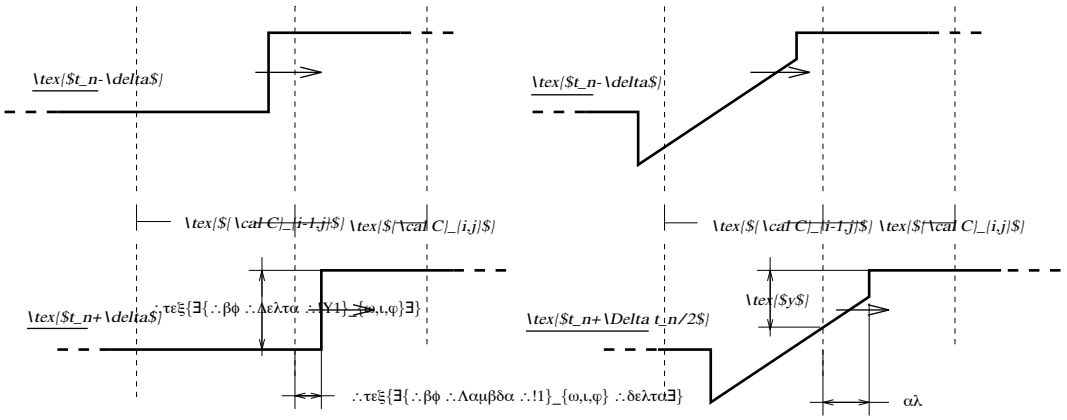

Figure 4: *propagation of piecewise constant (left) and linear waves (right)*

Thus, taking into account the effects of all (modified) wave (forms) crossing the $\partial\mathcal{C}1_{i,j}$ cell interface at time t_n and propagating with local speed $\mathbf{\Lambda 1}_{p,i,j}$ one obtains, for $\mathbf{F1}_{i,j}$

$$\mathbf{F1}_{i,j} = \mathbf{f}(\mathbf{U}^n_{i,j}, \mathbf{n}(\mathbf{x}_p)) - \sum_{p=1}^{np} \mathbf{\Lambda 1}^+_{p,i,j}\mathbf{\Delta U1}_{p,i,j} - \frac{1}{2}\sum_{p=1}^{np} |\mathbf{\Lambda 1}_{p,i,j}|\mathbf{\Delta U1}_{p,i,j}(\mathbf{I}l1_{k,j} - |\mathbf{\Lambda 1}_{p,i,j}|\Delta t_n)\mathbf{\Sigma 1}_{p,k,j} \tag{12}$$

where $k = i-1$ if $\mathbf{\Lambda 1}_{p,i,j} > 0$ and $k = i$ otherwise. Notice that in (12) the (downwind) effects due to the propagation of a piecewise linear wave form out of the $\mathcal{C}_{i,j}$ cell have also been accounted for. The slopes $\mathbf{\Sigma 1}_{p,k,j}$ over the $\mathcal{C}_{k,j}$ cell are computed comparing the jumps $2\mathbf{\Delta U1}_{p,k,j}/(l1_{k-1,j}+l1_{k,j})$ and $2\mathbf{\Delta U1}_{p,k+1,j}/(l1_{k,j}+l1_{k+1,j})$ across the same waves at the $\partial\mathcal{C}1_{k,j}$ and $\partial\mathcal{C}1_{k+1,j}$ the cell interfaces through the van Leer limiter function. One can show that, for the one dimensional linear case and taking local slopes, then $\mathbf{F1}_{i,j}$ as defined in (12) is a second order approximation to the flux function $\mathbf{f1}_{i,j}$. Clearly $\mathbf{F1}_{i,j}$ is also consistent with the flux function $\mathbf{f}$. Thus the approximate solution of Riemann problems at each cell interface provides all the ingredients (jumps and speeds of the waves) we need to compute the numerical fluxes and we can write the finite volume high resolution method as follows:

$$\mathbf{U}^{n+1}_{i,j} = \mathbf{U}^n_{i,j} - \frac{\Delta t_n}{S_{i,j}}[h1_{i+1,j}\mathbf{F1}_{i+1,j} - h1_{i,j}\mathbf{F1}_{i,j}] - \frac{\Delta t_n}{S_{i,j}}[h2_{i,j+1}\mathbf{F2}_{i,j+1} - h2_{i,j}\mathbf{F2}_{i,j}] \tag{13}$$

where $\mathbf{F1}_{i+1,j}$, $\mathbf{F2}_{i,j+1}$ and $\mathbf{F2}_{i,j}$ are given by expressions similar to (12). Actually a Strang splitting ([6] pp. 202-205) version of (13) has been used.
Let $I1(\Delta t_n)$ and $I2(\Delta t_n)$ be the operators updating the cell averages $\mathbf{U}_{i,j}$ by accounting for the fluxes across the $\partial\mathcal{C}1_{i,j}$ and $\partial\mathcal{C}2_{i,j}$ cell interfaces over the time interval Δt_n:

$$I1(\Delta t_n) \; : \quad \mathbf{U}_{i,j} \; \rightarrow \; \mathbf{U}_{i,j} - \frac{\Delta t_n}{S_{i,j}}[h1_{i+1,j}\mathbf{F1}_{i+1,j} - h1_{i,j}\mathbf{F1}_{i,j}] \tag{14}$$

$$I2(\Delta t_n) \; : \quad \mathbf{U}_{i,j} \; \rightarrow \; \mathbf{U}_{i,j} - \frac{\Delta t_n}{S_{i,j}}[h2_{i,j+1}\mathbf{F2}_{i,j+1} - h2_{i,j}\mathbf{F2}_{i,j}] \tag{15}$$

then the cell averages at the time t_{n+k} are computed, starting from the initial data $\mathbf{U}^n_{i,j}$, according to the following rule

$$\begin{aligned}\mathbf{U}^{n+k}_{i,j} = {} & I2(\frac{\Delta t_n}{2}) \circ I1(\Delta t_{n+k-1}) \circ I2(\Delta t_{n+k-2}) \circ \cdots \\ & \cdots \circ I2(\Delta t_{n+3}) \circ I1(\Delta t_{n+2}) \circ I2(\Delta t_{n+1}) \circ I1(\Delta t_{n+1}) \circ I2(\frac{\Delta t_n}{2}) \circ \mathbf{U}^n_{i,j}\end{aligned} \tag{16}$$

At each time step Δt_n is computed on the basis of a one dimensional CFL rule and reduced of 10%

$$\Delta t_n = 0.9 \min_{\substack{i=1,nc1 \\ j=1,nc2}} \left(\frac{l1_{i,j}}{(a_{i,j} + (\mathbf{v}_{i,j}\cdot\mathbf{v}_{i,j})^{1/2})}, \frac{l2_{i,j}}{(a_{i,j} + (\mathbf{v}_{i,j}\cdot\mathbf{v}_{i,j})^{1/2})}\right), \qquad \begin{matrix} a_{i,j} = a(\mathbf{U}^*_{i,j}) \\ \mathbf{v}_{i,j} = \mathbf{v}(\mathbf{U}^*_{i,j}) \end{matrix}$$

$$\mathbf{U}^*_{i,j} = I1(\Delta t_{n-1}) \circ I2(\Delta t_{n-1}) \circ \cdots \circ I2(\Delta t_1) \circ I1(\Delta t_1) \circ I2(\Delta t_0/2)\mathbf{U}^0_{i,j} \tag{17}$$

where $a(\mathbf{U}^*_{i,j})$ is the speed of sound computed with the $\mathbf{U}^*_{i,j}$ cell averages.

Mesh and initial condition; the problem of symmetry.
Most computations have been made on the O-mesh proposed in [3]. This has 32 cells in the radial and 128 cells in the tangential direction. The cells are angularly equally distributed and radially clustered on the circular cylinder according to the rule:

$$\rho_1 = .5 \qquad \rho_j = .5\,(1 + \sum_{k=0}^{j-2} \alpha^k \frac{2\pi}{128}) \qquad j = 2, \ldots, 33 \qquad \alpha = 1.1648336$$

Beside this standard mesh ($M0$) a 64×256 ($M1$) and a 128×512 ($M2$) ones have been used. Both are refinements of $M0$.

We consider two different initial conditions; a first one, symmetrical with respect to the x-axis is defined, for a given value of M_∞ as follows:

$$\mathbf{U}^0_{i,j} = \begin{pmatrix} 1 \\ \sqrt{\gamma} M_\infty \\ 0 \\ 1/(\gamma-1) + \gamma/2 M_\infty^2 \end{pmatrix} \qquad \begin{matrix} i = 1, \ldots, nc1 \\ j = 1, \ldots, nc2 \end{matrix}$$

A second initial condition is obtained by the first one by asymmetrically perturbing the values of the first component of $\mathbf{U}^0_{1,nc2}$ and $\mathbf{U}^0_{nc1,nc2}$ by $+10^{-6}$ and -10^{-6} respectively. These are the values of the density in the two cells bounded both from the x-axis and from the outer boundary in the rear part of the cylinder.

In the numerical experiments we first compute, for a given value of M_∞, the symmetrical solution by starting the time integration from the symmetrical initial condition. Then we repeat the computation starting this time from the asymmetrically perturbed initial data. For both computations we use the same grid and the same code. It has been written to provide, for symmetrical initial data, symmetric updated values of the cell averages. This can be achieved by making sure that at each time step the computation of symmetric objects (normal vectors, fluxes, slopes, etc.) is performed on the basis of the same sequence of operations (but with different operands, of course!). This is a necessary condition since $a+b+c = a+c+b$ does not always hold in computer arithmetic. It is of course also sufficient if the operands are symmetric.

Boundary conditions.
At the surface of the cylinder the wall boundary condition $\mathbf{v} \cdot \mathbf{n} = 0$ is indirectly enforced through the definition of a proper Riemann problem. Let $\mathbf{n}$ be oriented inwards the computational domain and $\mathbf{t}$ normal to $\mathbf{n}$. Consider one of the $\partial\mathcal{C}2_{i,1}$ cells interfaces laying on the surface of the circular cylinder. At each time step let $\mathbf{U}^n_{i,0}$ and $\mathbf{U}^n_{i,1}$ be the initial data on the left and on the right sides of the $\partial\mathcal{C}2_{i,1}$ cell interface respectively. Let

$$\mathbf{U}^n_{i,0} = \begin{pmatrix} \rho^n_{i,0} \\ \rho^n_{i,0}\mathbf{v}^n_{i,0} \\ \rho^n_{i,0}e^n_{i,0} \end{pmatrix} \quad \Big| \quad \begin{matrix} \rho^n_{i,0} = & \rho^n_{i,1} \\ \mathbf{v}^n_{i,0}\cdot\mathbf{n} = & -\mathbf{v}^n_{i,1}\cdot\mathbf{n} \\ \mathbf{v}^n_{i,0}\cdot\mathbf{t} = & \mathbf{v}^n_{i,1}\cdot\mathbf{t} \\ e^n_{i,0} = & e^n_{i,1} \end{matrix} \quad , \quad \mathbf{U}^n_{i,1} = \begin{pmatrix} \rho^n_{i,1} \\ \rho^n_{i,1}\mathbf{v}^n_{i,1} \\ \rho^n_{i,1}e^n_{i,1} \end{pmatrix} \tag{18}$$

it is easy to see that, because of the symmetry of this R.p., the wall boundary condition is satisfied for the intermediate state at the cell interface. Some care must be taken to maintain on this boundary the same accuracy as at the internal cell interfaces. This can be achieved by considering, on the (pseudo) cell $\mathcal{C}_{i,0}$, slopes $\mathbf{\Sigma 2}_{p,i,0}$ which can be computed by reflecting the $\mathbf{\Sigma 2}_{p,i,1}$ ones in the same fashion as in (18). Thus the cell interfaces lying on the surface of the cylinder can be treated as the internal ones as it must be since a wall is a *natural* boundary.

Consider now the $\partial\mathcal{C}2_{i,nc2+1}$ interfaces laying on the outer boundary. For these we apply the boundary conditions discussed in [9] and originally proposed in [10]. We must distinguish between the cases of an *inlet* and of an *outlet* cell interface. Through the first one the gas flows from outside into the computational domain $\mathcal{C}$. For this case the intermediate state $\mathbf{u}(\mathbf{x}_p, t_n)$ is evaluated by imposing the total enthalpy, the entropy and the direction of the velocity $\mathbf{v}$ of the free stream together with the relationships which are compatible with the wave configuration of fig.5 left.

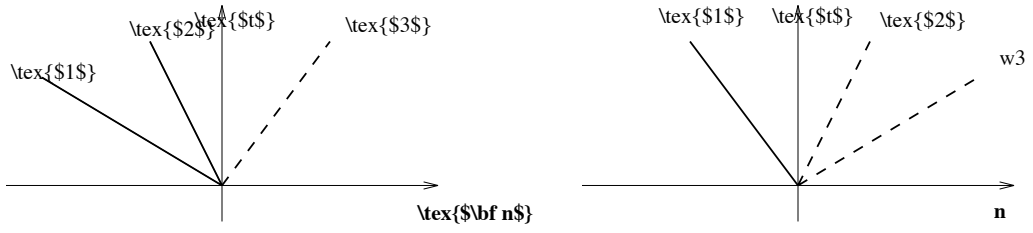

Figure 5: *wave configuration at inlet (left) and outlet (right) boundaries*

This is the wave configuration which is expected to come out of the breakdown of a discontinuity across a (inlet) cell interface whose right state is unknown. The wave 1 can be either a rarefaction wave or a shock whereas the wave 2 must be a contact discontinuity. In a similar way at *outlet* cell interfaces the exit pressure has been imposed (fig.5 right). This has been taken to be the pressure of the free stream. Both for inlet and for outlet cell interfaces no attempt has been made to correct the direction of the flow and the exit pressure by taking into account some potential solution in the far field ([11]). This is because we want to avoid the boundary condition to depend on the solution itself. Thus we can be sure that, if unsteadiness will be observed, this is not related to the treatment of the boundary. Notice also that these (inlet) boundary conditions are homentropic and homenergetic.

3. Numerical results

Output variables.
In this section we will show pictures where lift and drag coefficients are plotted against time. These have been defined as follows:

$$C_D^n = \frac{2}{D\gamma M_\infty^2} \sum_{i=1}^{nc1} p(\mathbf{U}_{i,1}^n) n_x$$

$$C_L^n = \frac{2}{D\gamma M_\infty^2} \sum_{i=1}^{nc1} p(\mathbf{U}_{i,1}^n) n_y$$

where D is the diameter of the circular cylinder and p is the pressure computed with the cell averages of the $\mathcal{C}_{i,1}$ cell. No attempt has been made to extrapolate the pressure at the body. We also show the history of the density residual

$$\rho_{res}^n = \max_{1 \le i \le nc1} \sum_{j=1}^{nc2} |\rho(I1(\Delta t_n) I2(\Delta t_n) \mathbf{U}_{i,j}^*) - \rho(\mathbf{U}_{i,j}^*)|$$

$$\mathbf{U}_{i,j}^* = I1(\Delta t_{n-1}) \circ I2(\Delta t_{n-1}) \circ \cdots \circ I2(\Delta t_1) \circ I1(\Delta t_1) \circ I2(\Delta t_0/2) \mathbf{U}_{i,j}^0$$

moreover entropy and total enthalpy deviations has been defined as follows:

$$\Delta s_{i,j}^n = \frac{p(\mathbf{U}_{i,1}^n)/p_\infty}{(\rho(\mathbf{U}_{i,1}^n)/\rho_\infty)^\gamma} - 1$$

$$\Delta h_{0\,i,j}^n = \frac{h_0(\mathbf{U}_{i,1}^n)}{h_{0\infty}} - 1$$

Subcritical case.
In order to validate the numerical method and to quantify the errors due to the discretization we first consider the subcritical case $M_\infty = .38$. This computation was mandatory in [3]. As in [4],[13] and in the contributions C4, C5, C6, C14, C17, C18 and C20 of [3] we also found that the symmetrical (with respect to the x- axis) solution is steady, stable, without separation and circulating flow. Although a slight asymmetry with respect to the y-axis was observed. This is evident in the diagrams of fig.6 where the entropy (left) and the total enthalpy deviations (right) in the first row of cells surrounding the cylinder are plotted against the x-coordinate of the center of these cells. The three plots in each picture refers to computations made with the M0, the M1 and the M2 grids, as can be seen from the different density of output values. We recall that, for this case, both entropy and total enthalpy deviations (Δs and Δh_0) must be, in the exact solution, equal to zero. In [13] Di Mascio showed maximal values of Δs of about .01 for a finite volume method based on a second order approximation obtained through a predictor-corrector scheme. He also reported the results obtained with a first order Godunov's scheme ($\Delta s_{max} \approx .1$) and the ones computed with a MUSCL approach ($\Delta s_{max} \approx .03$). All these values refers to computations with a 32×128 grid. They should be compared with the ones shown in fig.6 (left) for a computation performed with the M0 grid.

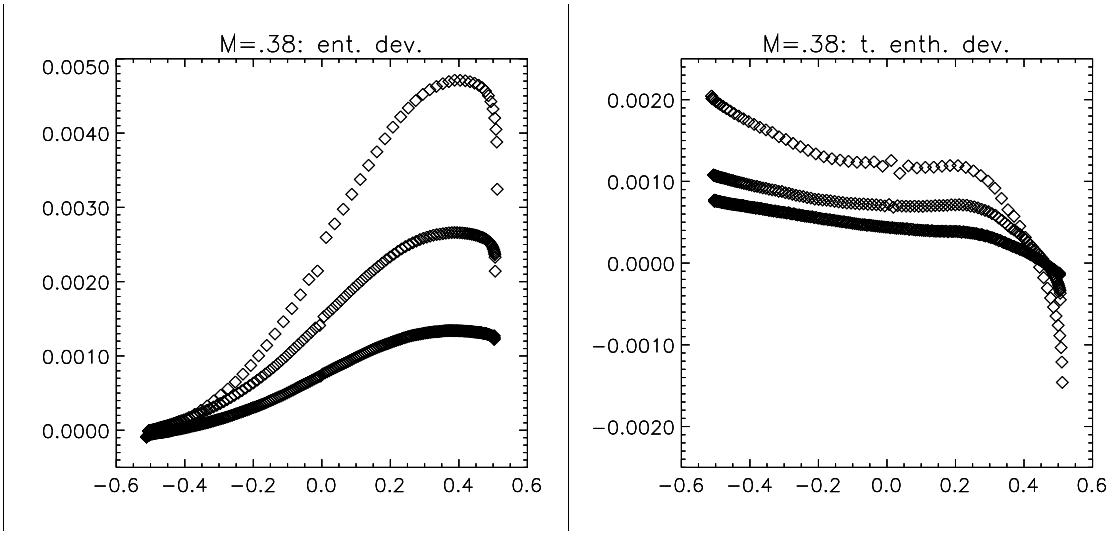

Figure 6: *subcritic case: entropy (left) and total enthalpy deviation (right) at the body*

Transonic cases.
Let us now turn to the $M_\infty = 0.5$ case. For this problem we remark a very good agreement between our computations and those presented in [4] and [13]. As Pandolfi and Larocca we also found the symmetrical solution to be periodic and unstable. Beginning the integration from the (asymmetrically) perturbed initial condition we noticed the growth of oscillations in the vortex sheet initially aligned with the centerline. After a transient (up to about 50 time unities) the transition to the asymmetric periodic solution was observed. In fig.7 and 8 the histories of drag and lift coefficients are shown for $t \in [0, 300]$ on the left and $t \in [540, 560]$ on the right. The computation was carried on for 80000 time steps up to $t \approx 600$ with the M0 grid (32×128). If we compare these two pictures with fig.5 of [4] we can see that, in spite of the differences in the transitory (essentially due to the different initial condition), the periodic path are very similar. Although in our computation the drag coefficient oscillates between 1.15 and 1.3 whereas in [4] oscillations between 1.17 and 1.5 were observed. This is probably due to the fact that our computation of C_D and C_L is based on the cell averages whereas in [4], because of the finite differences discretization, computational points were laying on the surface of the cylinder. In [13] Di Mascio shows C_D oscillations between 1.0 and 1.1. As mentioned he also used a finite volume method. Consider now fig.9. The C_D history is shown for a computation performed on the M1 grid (64x128). The integration was carried on until about 400 time unities. We point out the good agreement between the two computations (the C_L history has not been plotted since no appreciable differences between the two computations can be seen in this representation). Differently as in [4] we have not found, by refining the grid, a significant change in the amplitude of the C_D oscillations. Instead a smoother path was observed in the computation with the finer grid. No change in the frequency was noticed. We also notice that the C_D oscillations obtained in [4] with a 64×256 grid seems more in agreement with our computations than those obtained there with a 32×128 grid. To give an idea of the flow field a sequence of four instantaneous pressure coefficient contour lines has been shown in fig.11 for the computations made on the coarse grid. The time interval covered by these pictures is about one half of the period of the flow. Therefore after the last picture the same sequence is repeated on the upper side of the cylinder. These pictures should be compared with the ones of fig.7 in [4] to appreciate the agreement of the two computations and the regularity of the flow. We also refer to the work of Pandolfi and Larocca for a detailed description of the flow over a period. Let us strike the fact that we do not have seen any appreciable dependence of this periodic solution on grid refinement, time interval or initial condition.

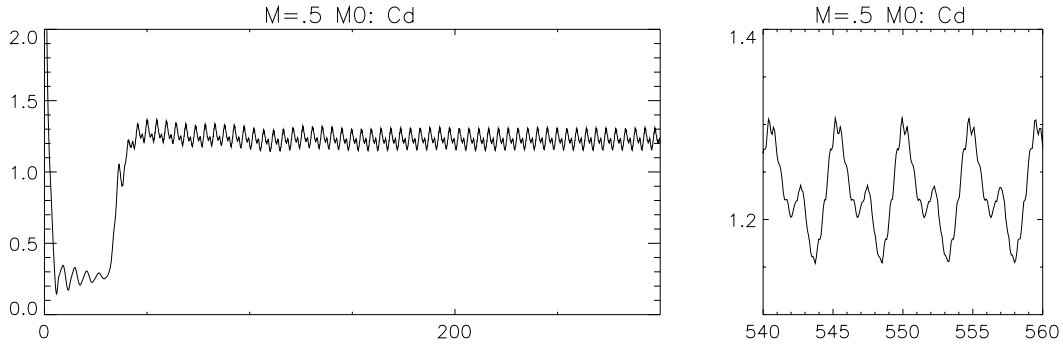

Figure 7: $M_\infty = 0.5$, *M0 grid; drag coefficient history*

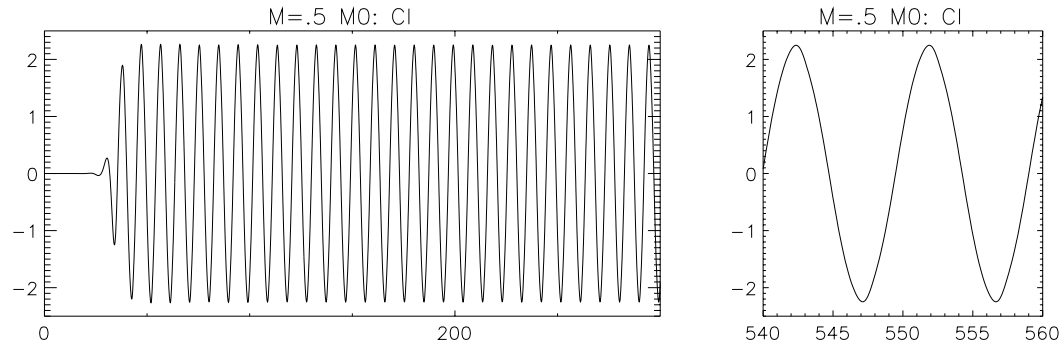

Figure 8: $M_\infty = 0.5$, *M0 grid; lift coefficient history*

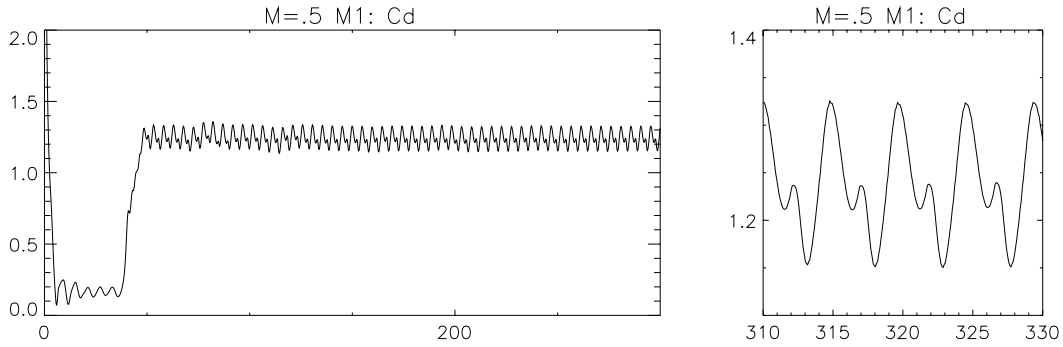

Figure 9: $M_\infty = 0.5$, *M1 grid; drag coefficient history*

We now increase the free stream Mach number up to 0.65. In fig.12 and 13 the C_D and C_L histories are reported for a computation on a M0 grid. By comparison between these and fig.7 and fig.8 we can notice that, increasing the M_∞,

i) the amplitude of the C_D oscillations increases and the one of C_L oscillations decreases.

ii) the frequency of C_L oscillations increases of about 50%. The frequency of the C_D oscillations does not change significantly.

iii) the length of the transient to reach the limit cycle increases.

Similar differences were found in [4] between the $M_\infty = 0.5$ and the $M_\infty = 0.6$ cases. Although there a reduction of the amplitude of the oscillation was observed *both* for C_D and C_L.

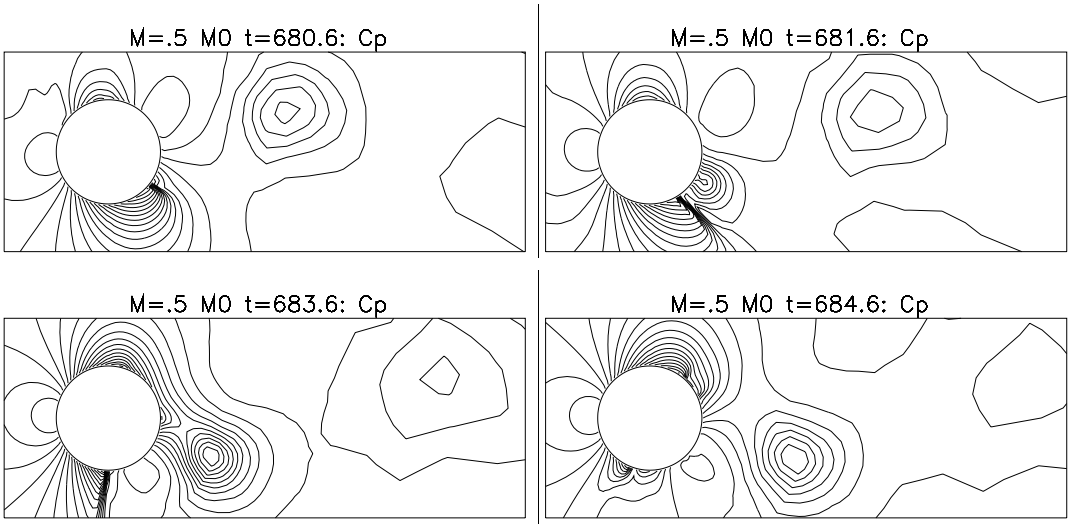

Figure 11: $M_\infty = 0.5$, *M0 grid; pressure coefficient contour lines*

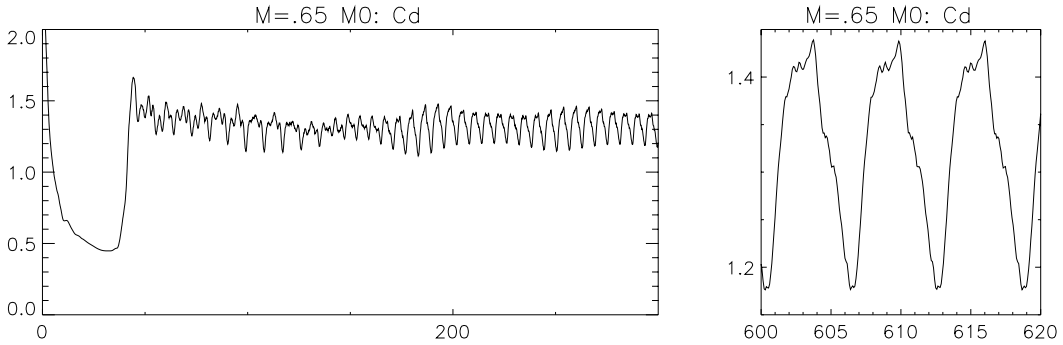

Figure 12: $M_\infty = 0.65$, *M0 grid; drag coefficient history*

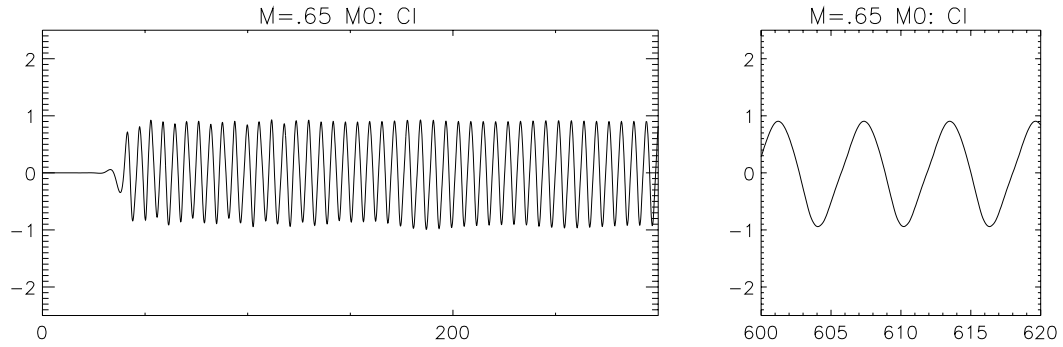

Figure 13: $M_\infty = 0.65$, *M0 grid; lift coefficient history*

Consider again the C_D path of fig.12 on the left. One can notice, beside the transient from the impulsively start up to the breakdown of the symmetry ($t \approx 50$) other two well defined time intervals. A first one characterized through irregular oscillations and then, at about $t = 150$, the transition to a different path. Here the C_D history seems to become periodic although through a modulated pattern. Further on the system approaches, at large times, a limit cycle where any information about the initial condition has been lost. In fact the path on the right side of the same picture (after about 80000 integration steps) is now perfectly periodic.

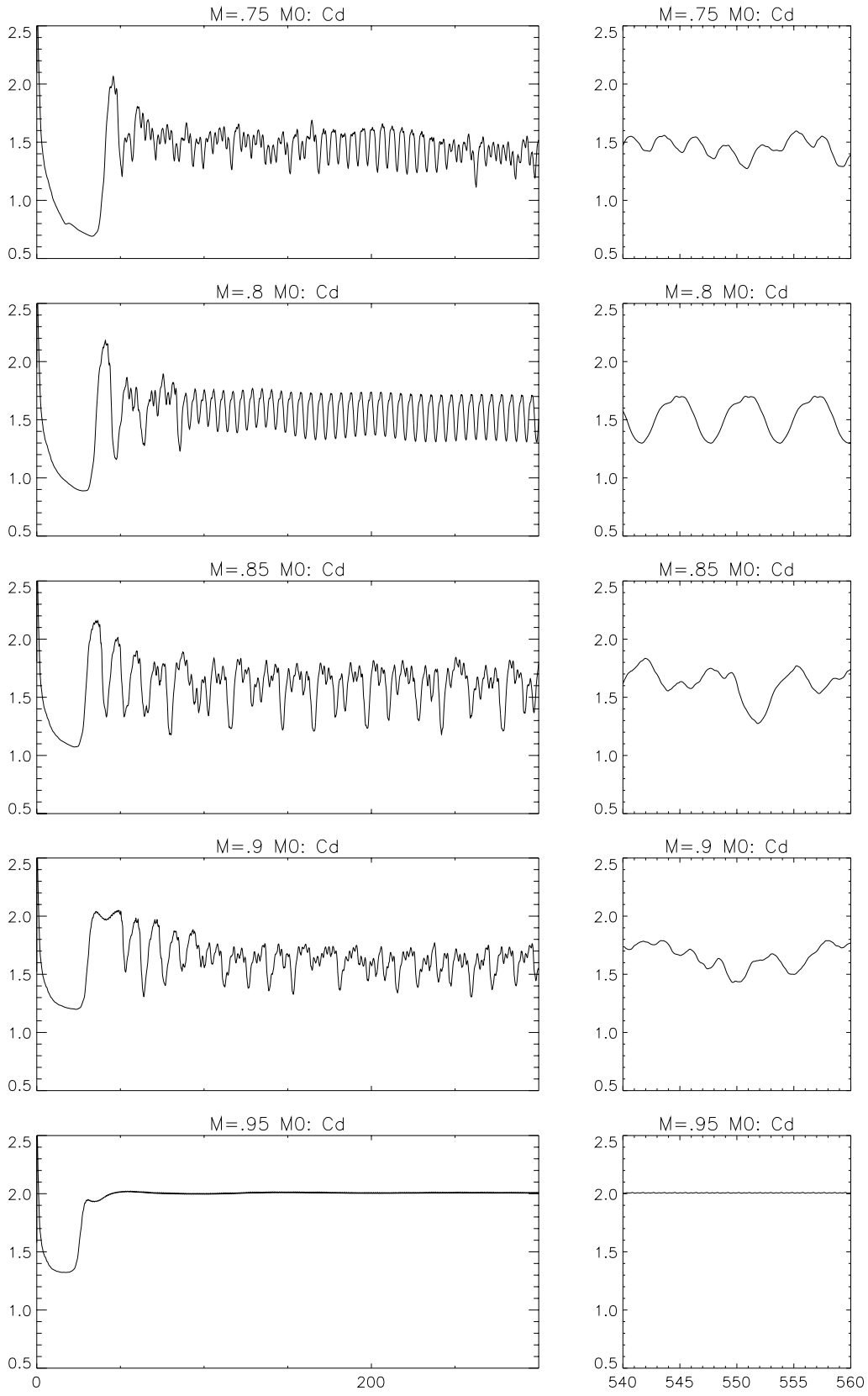

Figure 14: $0.75 \leq M_\infty \leq 0.95$, *M0 grid; drag coefficient history*

Let us now increase the M_∞ further. In fig.14 the C_D histories are compared for values of M_∞ between 0.75 and 0.95: Consider first the $M_\infty = 0.75$ case (fig.14 top). Here the flow exhibits a more complex behaviour. The solution fails to converge to a limit cycle; instead a broken, irregular pattern can be observed at large times. Inside this pattern some time intervals ($t \in [150, 250]$ and $t \in [800, 950]$, the last one not to be seen in fig.14) come out. These are displayed, with a different scale, in fig.15: the flow seems, for a while, to incline to a more regular behaviour and a periodical modulated pattern appears just as in the previous case. In spite of this it returns, at some later time, to a wild path of aperiodic oscillations.

Consider the second picture of fig.14. Here the C_D history refers to the $M_\infty = 0.8$ case. The flow reaches, after a transient which is even shorter than for the $M_\infty = 0.65$ case, a perfectly periodic solution ! Nevertheless a further increase of the M_∞ by 0.5 (third picture of fig.14 from the top) again brings a similar behaviour as for the $M_\infty = 0.75$ case with an increase of the amplitude of the oscillations. The same behaviour can be observed for the $M_\infty = 0.9$ case. Then, at $M_\infty = 0.95$, something new happens (fig.14 bottom). The flow returns to a (nearly) steady state solution characterized by a low amplitude high frequency oscillation of the C_D around a quite high value. This last transition is easy to understand on the basis of the two pictures represented in fig.16. On the left the instantaneous contour lines of the pressure coefficient for the flow at $M_\infty = 0.9$ have been plotted after a quite long time from the beginning of the integration. On the right the same output is shown for the $M_\infty = 0.95$ case. Even if the picture on the left is nothing but an instantaneous portrait of the flow, though the shock wave structure can be seen to be similar to the one observed at lower free stream Mach numbers: two primary radial shocks oscillating on the sides of the circular cylinder and shedding vorticity into the wake. This is true up to a small but significant detail. Observe the tip of the radial shock on the lower side of the circular cylinder (fig. 16 left). This joins, about one radii downstream, a region where the clustering of the contour lines reveals the presence of a shock about normal to the bulk of the stream. This detail of the flow field reveals the transition to a new wave configuration. This last is now completely developed in the flow at $M_\infty = 0.95$. Consider fig.16 (right) and the two pictures of fig. 18. Here we recognize the shock wave pattern typical for $M_\infty \to 1$: The two radial shocks have moved towards the rear part of the circular cylinder. They are still quite strong at the surface of the body but, after a short radial extension, their strength vanishes and they propagate as acoustic signals in a supersonic field. Behind these two shocks the flow separates. The contact surfaces coming out of the separation points converge towards the centerline about one radius downstream of the cylinder. Here one can see the formation of two oblique shocks. Across these the velocity returns almost parallel to the centerline, though still supersonic.

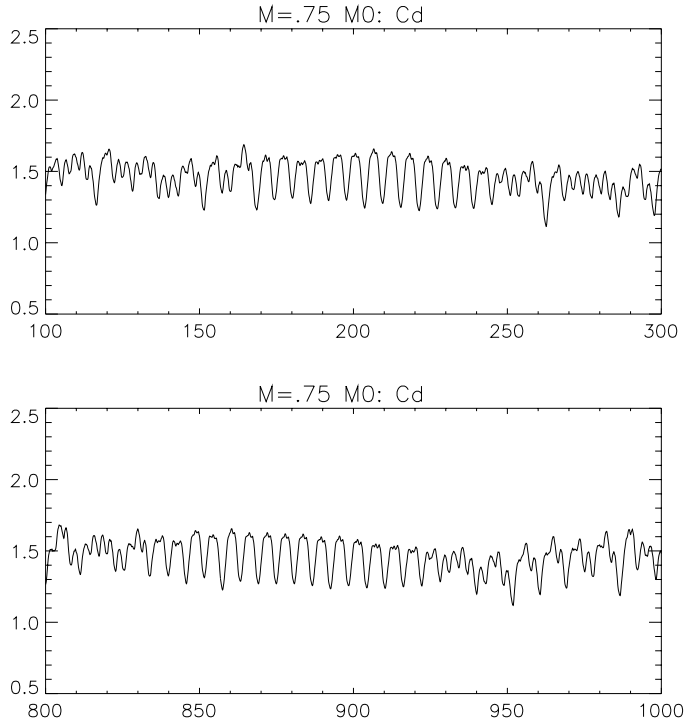

Figure 15: *$M_\infty = 0.75$, M0 grid; drag coefficient history: enlargement*

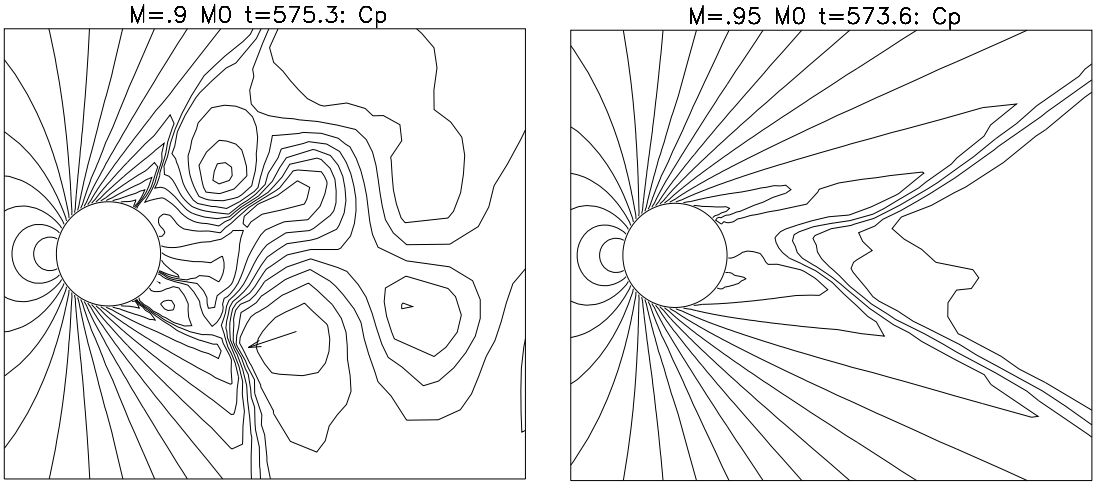

Figure 16: *$M_\infty = 0.9$, M0 (left) and $M_\infty = 0.95$, M0 (right); pressure coefficient contour lines*

After about four radii from the center of the cylinder the flow returns to the subsonic regime through a normal shock. This joins, on the two sides of the wake, the oblique shocks in two triple points. This shock wave structure is usually called a λ-shock. Inside the region squeezed between the two separation lines rising from the surface of the cylinder and the stagnation point in the wake the vorticity generated by the shocks at the surface is trapped in two oscillating circulating bubbles (fig.17). These bubbles form, together with the circular cylinder, the (equivalent) body which shapes the shock wave structure. Thus the oscillation is confined in a narrow region of the rear part of the cylinder and the amplitude of the oscillations is drastically reduced. We point out the fact that both the λ-shocks and most of the primary radial ones are very weak. In fact an entropy plot would show that the dissipation is concentrated at the root of the primary shocks. This is also evident from the instantaneous velocity field of fig.18. Before turning to the problem of the aperiodic oscillations let us compare the shadowgraph of fig.18 left, revealing the density variations in a a $M_\infty = 0.98$ flow and our computation of the case $M_\infty = 0.95$ (right). As far as the shock structure is concerned, the agreement between our computation and the experiment is very good. The details of the flow in the wake are, in the experiment, shaped by the physical viscosity of the problem and therefore not reproducible in our (inviscid) computations.

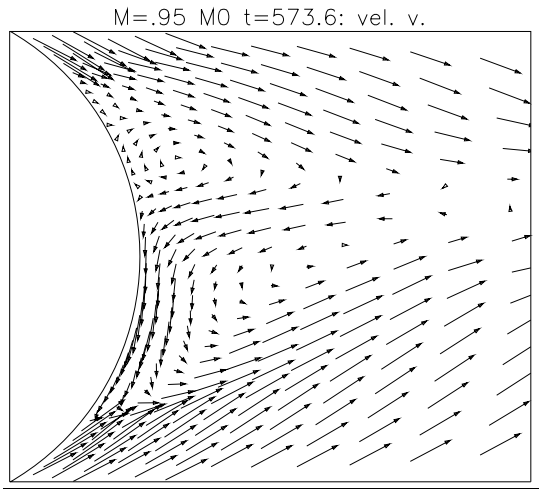

Figure 17: *$M_\infty = 0.95$, M0; velocity vectors in the circulating bubbles*

Aperiodic flow.

Let us turn the attention to the case of the irregular oscillations. In the rest of this section we want to discuss in some more detail the flow at $M_\infty = 0.85$. In the next two pictures we show, for both C_D and C_L, the paths obtained during the transition from the initial condition up to some time after the onset of the oscillating solution (left).

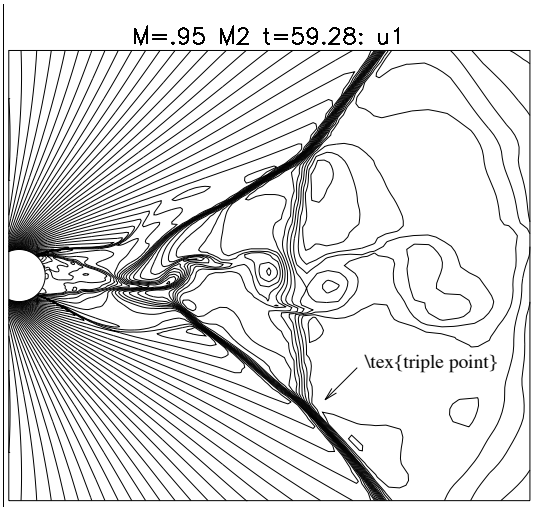

Figure 18: $M_\infty = 0.98$, *Dymentand, Gryson, Ducruet (left);* $M_\infty = 0.95$, *M2 grid (right)*

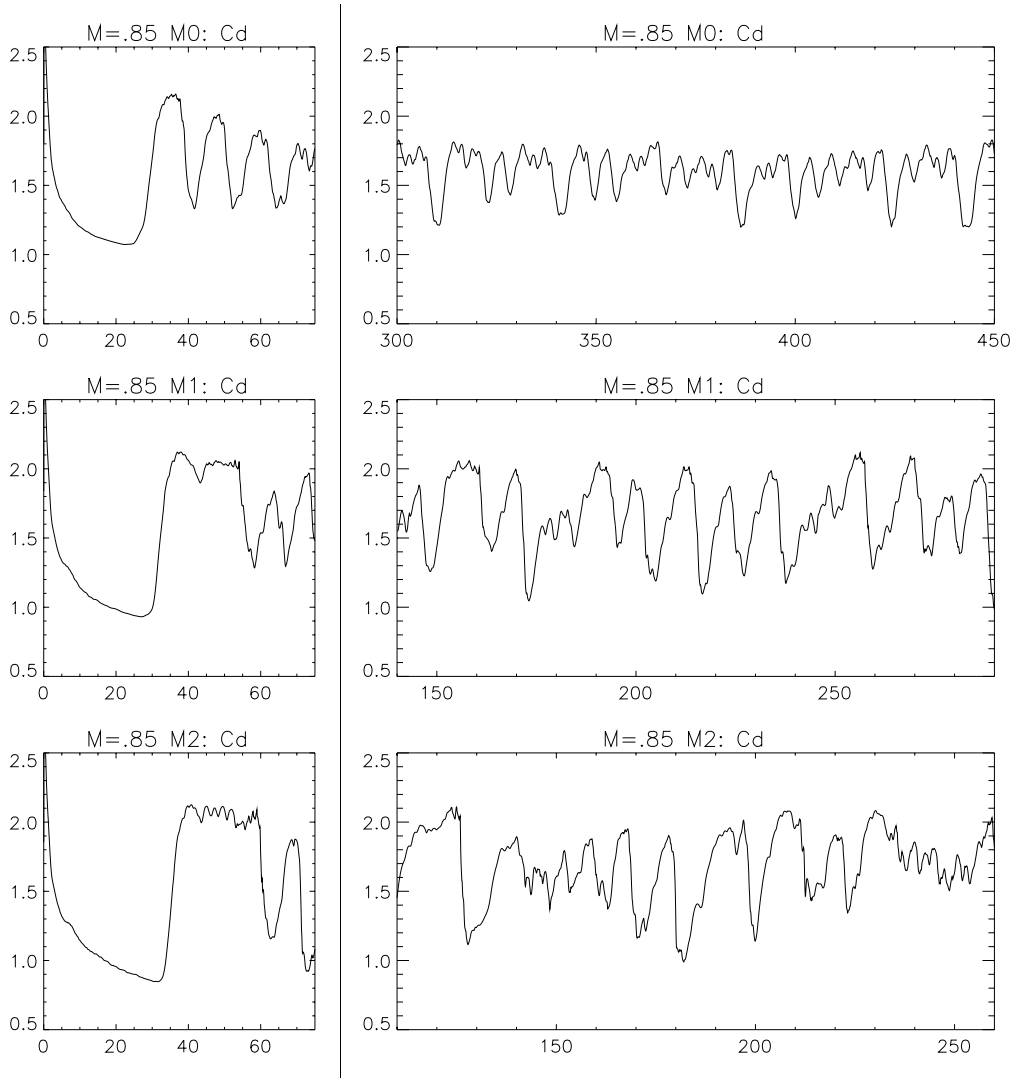

Figure 19: $M_\infty = 0.85$*;* C_D *history with M0, M1 and M2 grids*

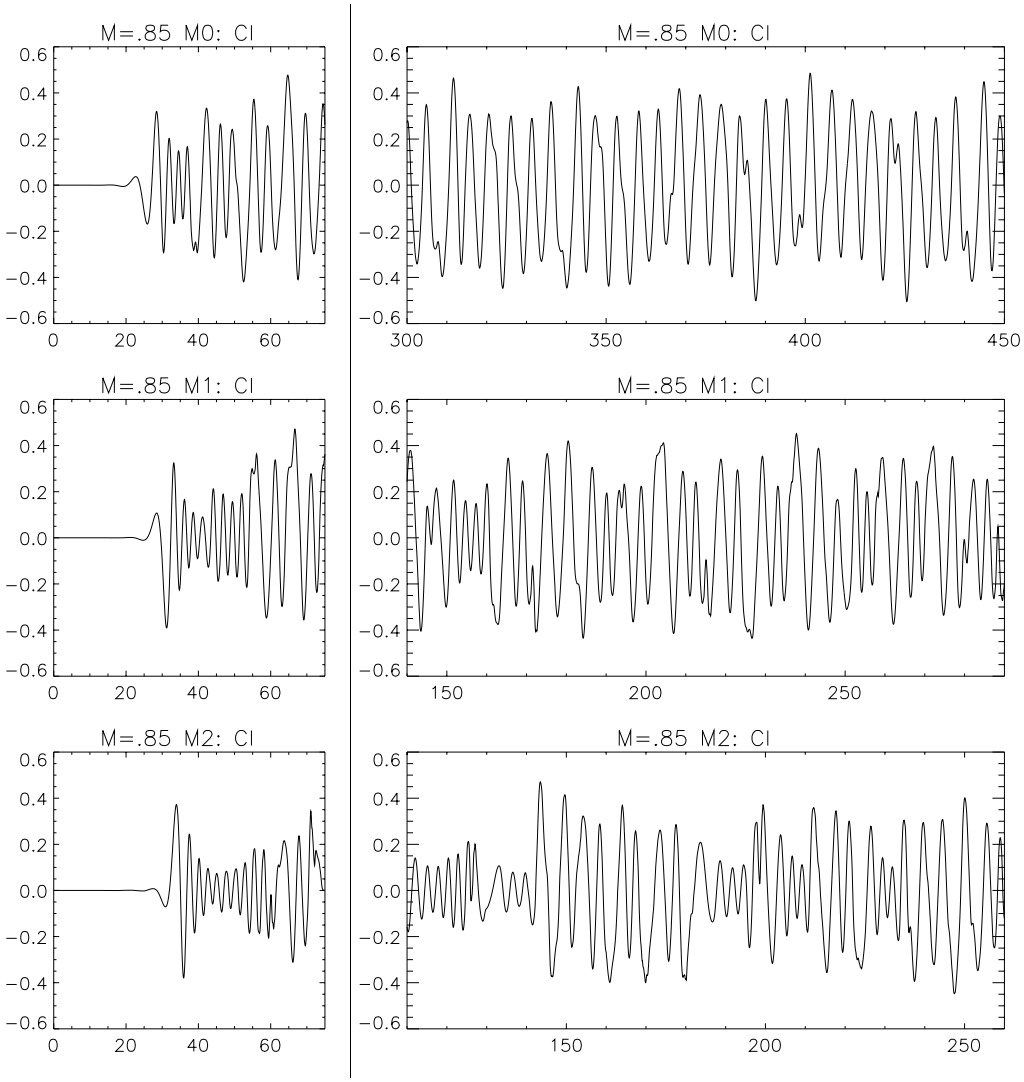

Figure 20: $M_\infty = 0.85$*; C_L history with M0, M1 and M2 grids*

On the right side of the same pictures the paths over a time interval of 150 unities after the irregular flow has developed have been shown. In each picture the results refer to the computations made with the M0 (top), M1 (middle) and M2 (bottom) grids. In the last case the integration was carried on just until $t \approx 150$. Consider first the time interval up to the break down of the symmetry (between 0 and about 25). Here we notice that, in spite of a slight decrease of the values of C_D with the successive refinements of M0, the agreement between the three computations is good. This is not any longer true after the onset of the oscillations. Also at large times (fig.19 right) the C_D histories computed with the M0 and with the M1 grids are different both in the amplitude of the oscillations and in the form of the irregular paths. We recall that, for the $M_\infty = .5$ case a perfect agreement was observed between the solutions obtained with the M0 and the M1 grids. In fig.19 we notice the tendency, for the flow computed with a finer grid, to persist for a longer time in some almost constant C_D configuration. This is particularly evident over the intervals $t \in [35, 60]$ and $t \in [80, 90]$. On these intervals also the C_L oscillations reduce from a high value to nearly zero. Consider fig.21 left. Here the pressure coefficient contour lines have been traced for the flow computed with the M2 grid and at $t = 83.95$. Output at $t \in [35, 60]$ would have shown similar results.

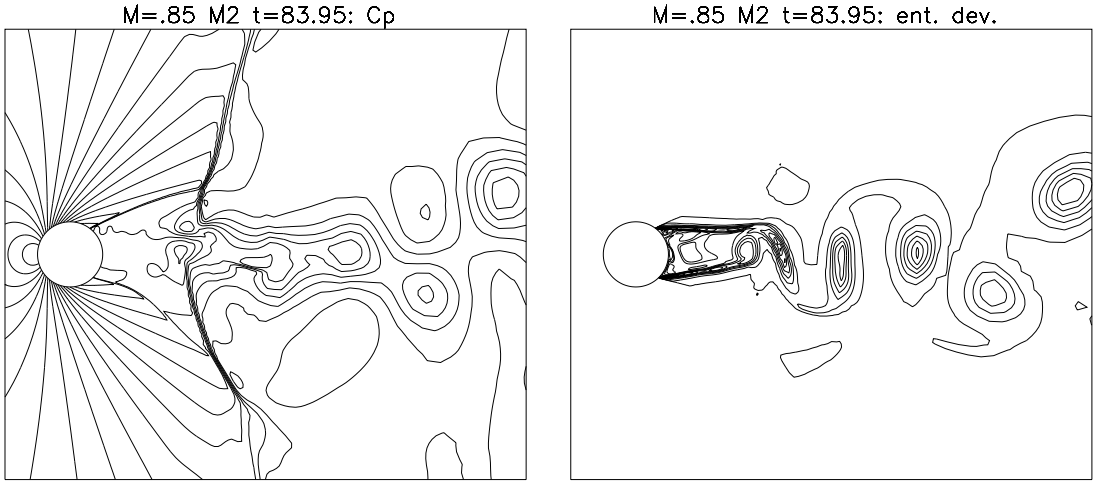

Figure 21: *$M_\infty = 0.85$, M2; pressure coefficient (left) and entropy deviation (right) contour lines*

The shock wave structure is some way related to the one depicted in fig.18 for the $M_\infty = 0.95$ case. The radial shocks surging from the two sides of the circular cylinder weaken after a short radial extension. They are weakly connected, at the triple points on the two sides of the wake, to another, nearly normal to the centerline one. Also the entropy contour lines at $t = 83.95$ are shown in fig.21 (right). The big, nearly round vortexes on the right side of this picture are the trace of a previous shock configuration with larger oscillations of the radial shocks. The vortex pattern near the cylinder, though, is similar to the one for $M_\infty \to 1$. The circulating bubbles are stretched and squeezed in the narrow region behind the cylinder. Although, let us point out an important difference between this case and the $M_\infty = 0.95$ one. Here vortexes are shed into the wake; there the circulating bubbles seemed not to detach and the wake downstream the cylinder was more similar to a thin vortex layer than to a vortex street. We can describe the evolution of this flow by considering the C_D and C_L paths enlargements of fig.22 together with the sequence of instantaneous contour lines of fig.23, 24, 25, 26 and 27. These cover a time interval of about 40 unities. Consider first fig.22. We notice that, for t between 83.95 and about 91.5 the amplitude of the C_L oscillation is dramatically reduced. The C_D approaches a nearly constant value about 2. At $t = 89.37$ (first picture of fig.23) the flow structure is basically the same as in fig.21. Yet the region of circulating flow has become narrower and the normal shocks in the wake of the circular cylinder stronger (entropy contour lines on the right side). The part of this shocks which is more closed to the centerline is bent toward the rear part of the cylinder in a fashion

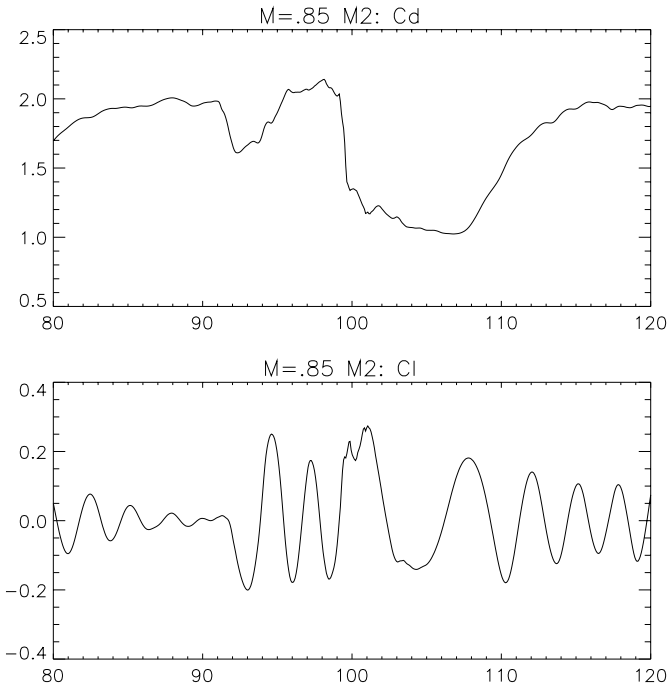

Figure 22: *$M_\infty = 0.85$, M2; C_D and C_L histories*

similar to the oblique shocks of fig.18. Also notice, in the entropy contour lines, that the big round vortexes at the right-hand side of the picture have disappeared (since they have been conveyed downstream) giving place to a narrower vortex street. At $t = 90.46$ the λ-shock structure of the $M_\infty \to 1$ configuration appears on the upper side of the circular cylinder. This structure is not stable.

This is due to the fact that, differently than in the $M_\infty \to 1$ case, highly rotational vortexes are shed into the wake and conveyed through the region between the centerline and the upper triple point. As one can see from the third picture of fig.23 this triple point has disappeared after about one time unit. Instead a symmetrical one was born in the lower side of the wake. Thus at t about 91 the flow has reached, for a while, a configuration which is very similar to the one shown in fig.18 and corresponding to the quasi steady $M_\infty \to 1$ flow. At this time the C_D coefficient is about 2 and the C_L about zero. In the sequence of pictures represented in fig.24, 25 and 26 we can see the breakdown of this configuration. First the quasi symmetry with respect to the x-axis is lost: At $t = 92.64$ the radial shock on the upper side of the cylinder has moved upstream generating a big vortex on its high pressure side. After about one time unit this shock has lost its connection to the almost normal shock in the rear part of the flow (second picture of fig.24). At the same time the other radial shock on the lower side of the cylinder moves upstream too. Consider the flow at $t = 94.82$: on one side one can observe, in the wake downstream the cylinder, a complex interaction of the rests of the weak $M_\infty \to 1$ shock wave pattern. On the other side the oscillating radial shocks give rise, in the vicinity of the body, to a flow similar to the one that can be observed in the low transonic regime. In fact, between $t = 91.54$ and $t = 94.82$, the system has made about one pseudo oscillation (see also the C_L path of fig.22) and two counter rotating vortexes have been shed into the wake. These are named, in the entropy deviation contour lines of fig.24, V_u^0 and V_d^0. The upper one rotates clockwise. It has been generated by the radial shock on the upper side of the cylinder. Consider the interaction of these two vortexes with the two small ones (V_u^{-1} and V_d^{-1}) just in the middle of the same picture. They are a rest of the previous oscillation of the flow around the $M_\infty \to 1$ configuration, as one can realize from the previous pictures. The lower one (V_d^{-1}) rotates counterclockwise whereas the middle one (V_u^{-1}) rotates just as V_u^0. Consider fig.25: The V_u^{-1} vortex slides out of the layer between V_u^0 and V_d^{-1} and is rolled up by V_u^0 ($t = 95.90$). After about one time unit the two clockwise rotating vortexes has joined together to form a stronger one on the upper side of the wake ($t = 96.98$). Notice how the structure of both V_u^0 and V_u^{-1} can still be recognized inside $V_u^0 + V_u^{-1}$. Instead at $t = 98.06$ they have merged into a single vortex. Just the same happens to V_d^0 and V_d^{-1}. This last vortex is leapfrogged, in turn, by V_d^0. The two vortexes coalesce and the resulting one is conveyed downstream. This can be seen in the last picture of fig.25 and in the first frame of fig.26. Over the time interval covered by fig.24 and fig.25 the flow in the vicinity of the cylinder has made about two cycles of the pseudo oscillation generating thus two couples of counter rotating vortexes. These can be clearly seen in the first picture of fig.26. In this same figure we notice the onset of a new phase: The shock structure behind the circular cylinder get closed to the body; in the rear part of the cylinder we observe four radial shocks and a circumferential one (fig.26 middle and enlargement of this flow in fig.28): the last is due to the re-compression of the supersonic reversed flow generated by the two primary radial shocks. Also the other two radial shocks (which are more closed to the centerline) are generated by the re-compression of the same reversed flows. A velocity vector representation would reveal the instantaneous presence of four separation and four stagnation points on the surface of the cylinder. This complex configuration seems to slow down the oscillation of the two main shocks. In fact the C_L path remains, for t between 100 and about 101, at a nearly constant value. Also the entropy deviation contour lines of the last picture of fig.26 (whose enlargement has been used in the cover picture) shows that the generation of the lower counterclockwise rotating vortex takes more time that in the previous phase of the oscillation. From here on we observe the progressive degeneration of the shock structure in the rear part of the circular cylinder. A single low frequency oscillation of the two primary shocks produces, after about 10 time units, the flow represented in the first picture of fig.27 (see the C_L history of fig.22 between $t \approx 100$ and $t \approx 110$ too). Here no trace of the $M_\infty \to 1$ shock wave pattern behind the circular cylinder is left. Both the pressure coefficient and the entropy deviation contour lines reveal that the structure of the flow is controlled by the oscillation of the two radial shocks: they slowly move around a quasi steady configuration

alternately shedding vortexes in the wake. For $t > 110$ we observe once more that the amplitude of the oscillations get smaller and their frequency increases. The system undergoes a new transition which leads again to the onset of a $M_\infty \to 1$ configuration. This happens in much the same way as during the $[84, 94]$ time interval as one can see from fig.22 and from the second and the third pictures of fig.27. Note also the similarity between fig.21 and the last frame of fig.27.

Before trying to give an interpretation of these results let us stress the following points. The same behaviour as the one outlined above has been found, at large times too, both in the computations performed with the M1 and in the ones made with the M0 grids. In this last case, however, the coarseness of the grid does not allow a proper description of the λ-shocks downstream of the circular cylinder and the system seems to behave in a fashion which is more closed to the regular low transonic oscillations. This could also explain the qualitative differences between the C_D paths obtained, at large times, with M0 and M1 computations. As for the computation at $M_\infty = 0.5$ here also we have checked the influence of the time discretization on the numerical results. In the last picture the C_D and C_L histories for a computation performed with Δt_n reduced of 55% for the $M_\infty = 0.85$ case and with the M0 grid are shown. We point out the agreement between these results and the ones represented in figg.19 and 20 (top) for short times. At large times the two paths are still qualitatively very similar, yet quantitatively different: we observe here a dependence on the time discretization at large times.

Let us interpret the numerical results described in this section by means of the following conjecture: The transonic flow has, for a given value of M_∞ three solutions. A first symmetrical one which is always unstable. A second one which can be both stable or unstable depending on the value of M_∞: this is, in some phase space, the limit cycle corresponding to the periodical oscillation of the two radial shocks. A third one which also can be stable or unstable: this is the limit cycle (eventually contracting to a point for $M_\infty \to 1$) related to the λ-shock configuration shown in fig.18 for the $M_\infty = 0.95$ case. Thus, for values of the free stream Mach number in the low transonic regime, the third solution is unstable and the second one stable. On the other hand, when M_∞ is sufficiently closed to 1, the third solution becomes stable (and the second one unstable). Although there are values of M_∞ for which neither the second nor the third solutions are stable. In this case the flow oscillates (in the phase space) irregularly between these two (unstable) solutions. This is what happens for $M_\infty = 0.75$, $M_\infty = 0.85$ and $M_\infty = 0.9$.

4. Conclusions

We have closed the previous section with a conjecture about the kind of dependence of the solution on the control parameter M_∞. This conjecture is probably wrong. In fact the phenomena that we have described could be explained with many other assumptions. In spite of this our conjecture allows us to formulate the following important question:

Is *this* dependence of the solution on M_∞ just a feature of the numerical model or a characteristic of the Euler equation themselves? An answer to this question can just come from (numerical) experiments or from a deeper knowledge of the features of the mathematical model. Although we do not know other examples of compressible inviscid flow where these transitions have been observed, we think that this answer is positive and that the Euler equations exhibit, for this physical problem, a turbulent behaviour.

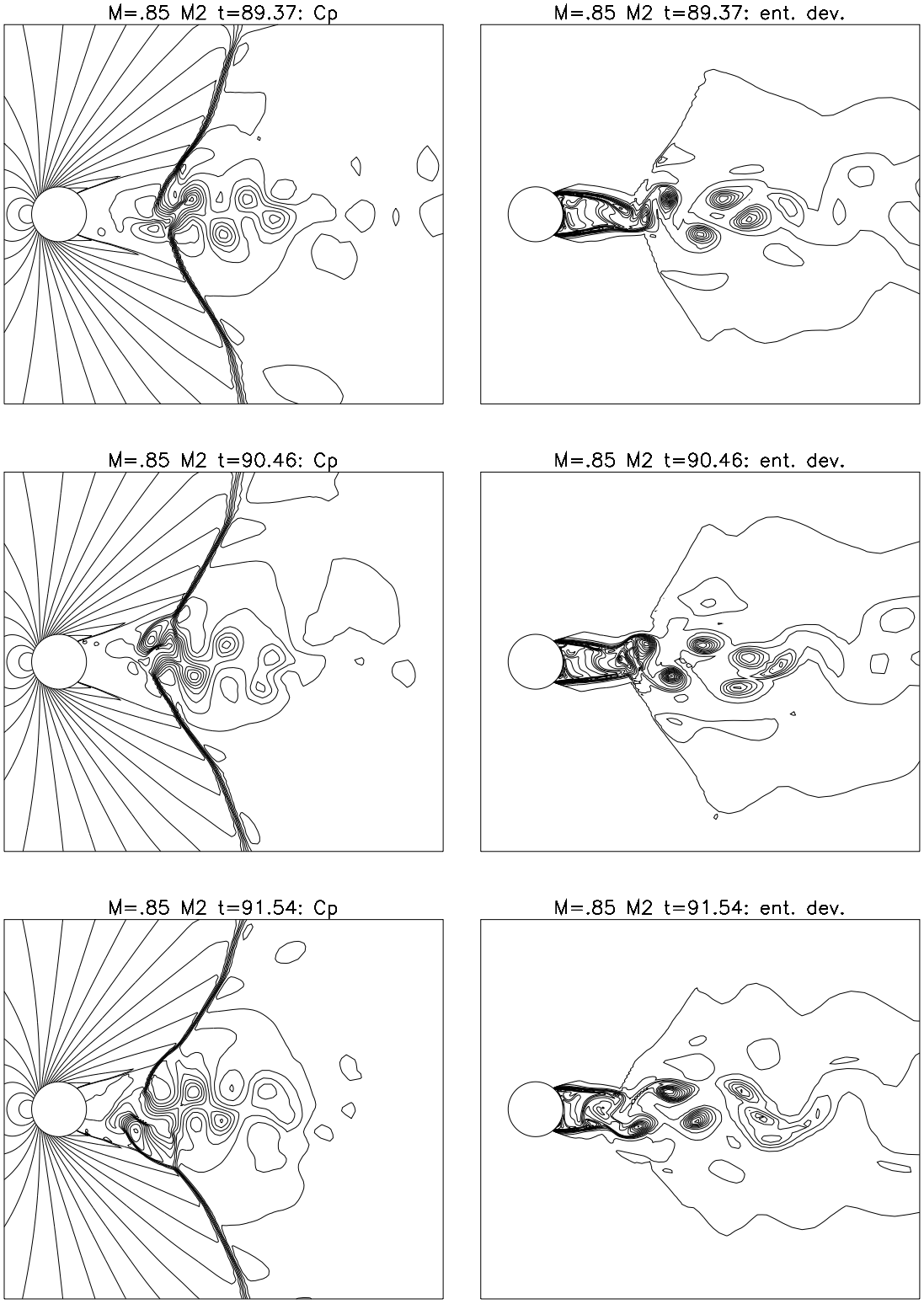

Figure 23: *$M_\infty = 0.85$, M2; pressure coeff. (left) and entropy deviation (right) contour lines. The flow approaches the $M_\infty \to 1$ configuration*

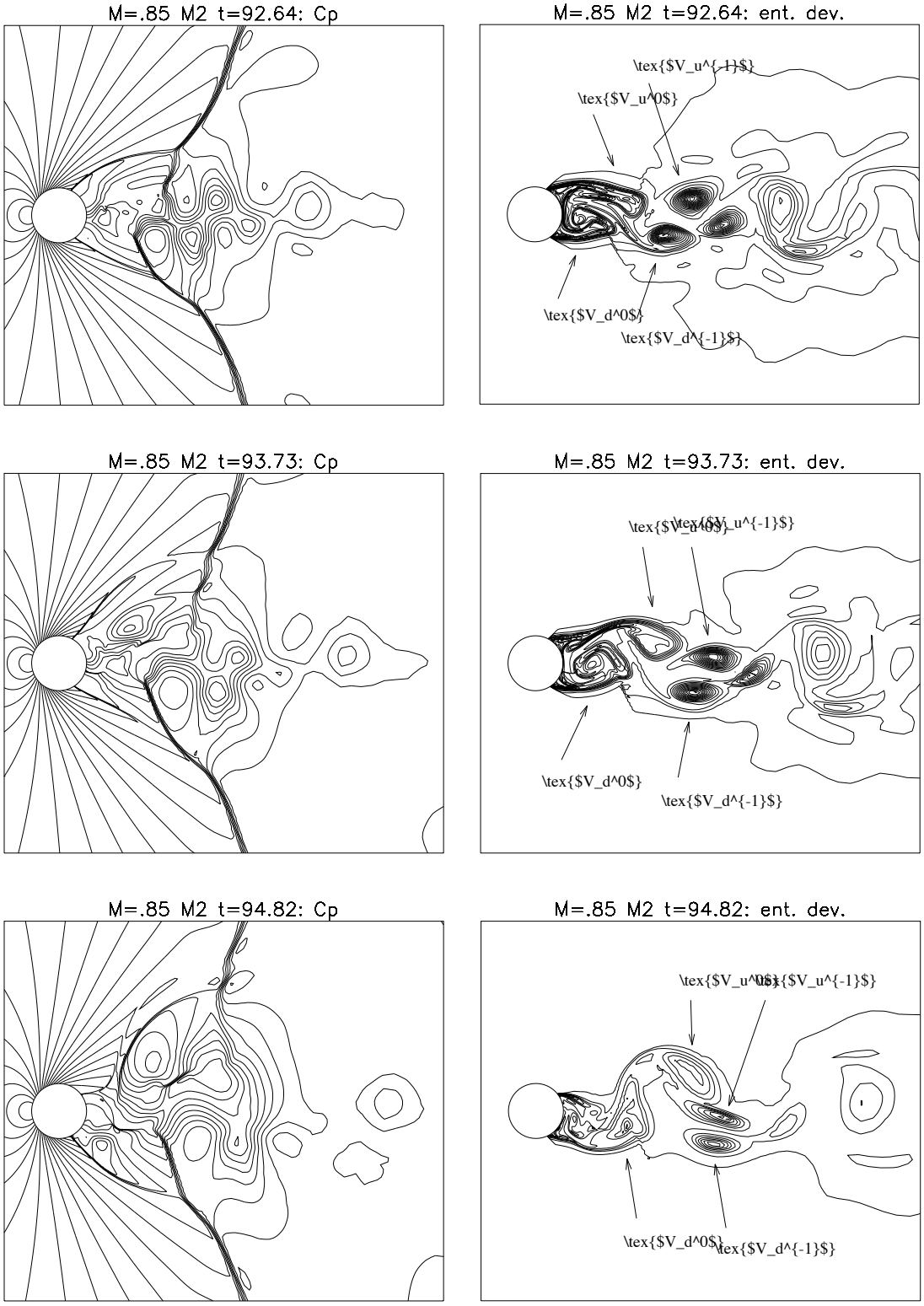

Figure 24: *$M_\infty = 0.85$, M2; pressure coeff. (left) and entropy deviation (right) contour lines. Breakdown of the $M_\infty \to 1$ configuration: the radial shocks begin to oscillate*

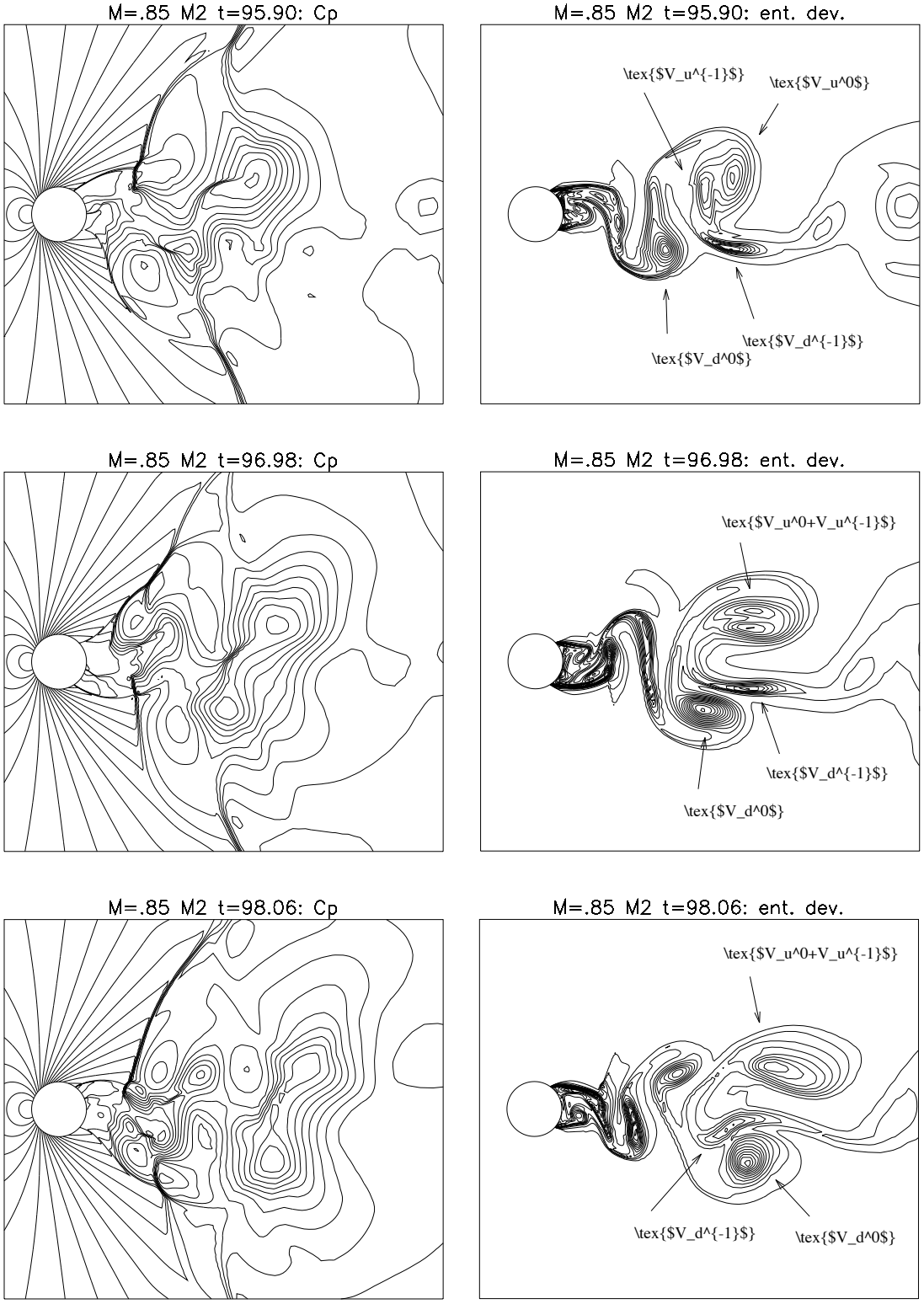

Figure 25: *$M_\infty = 0.85$, M2; pressure coeff. (left) and entropy deviation (right) contour lines. Breakdown of the $M_\infty \to 1$ configuration: the shock wave structure get closed to the rear part of the cylinder*

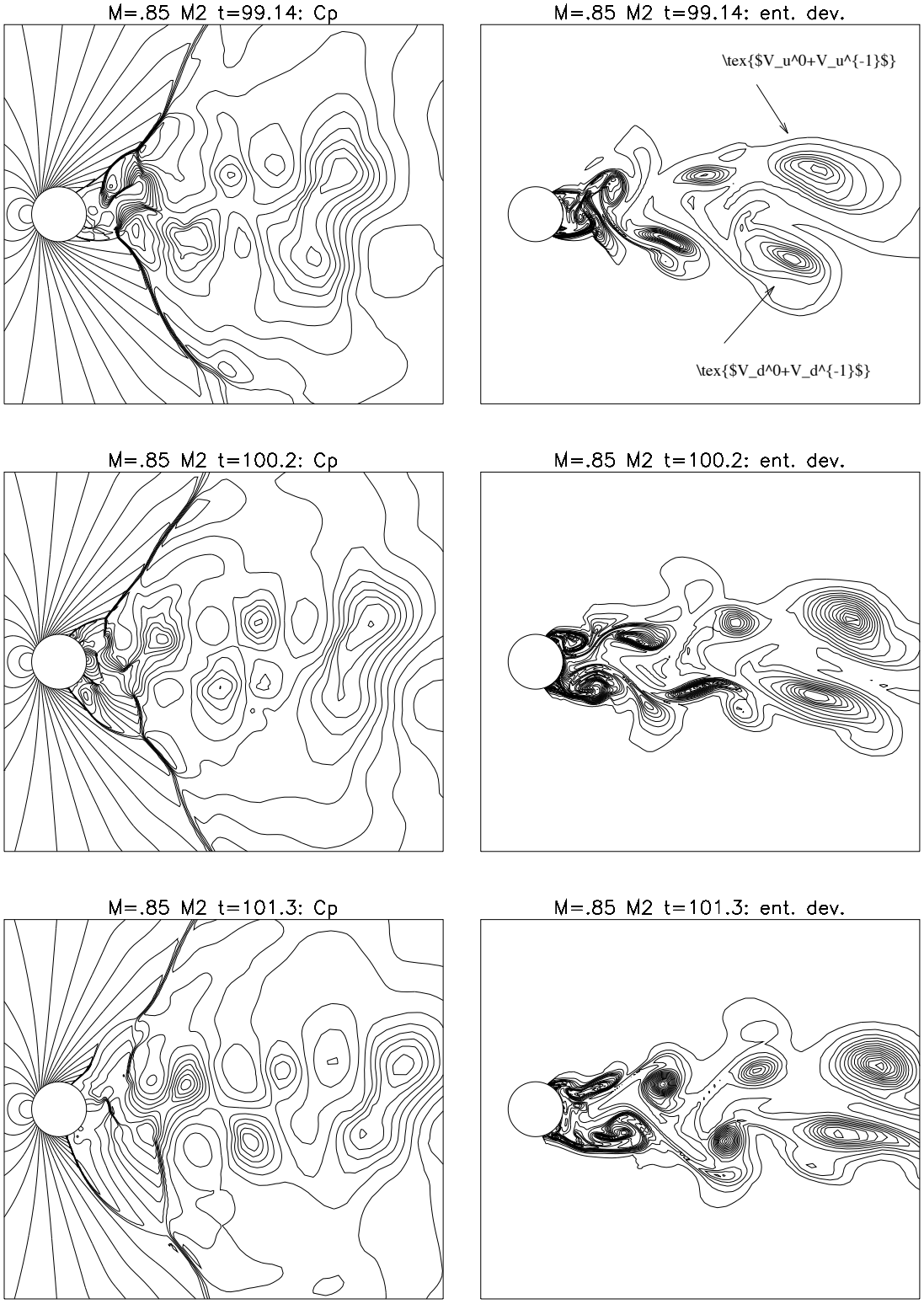

Figure 26: *$M_\infty = 0.85$, M2; pressure coeff. (left) and entropy deviation (right) contour lines. Breakdown of the $M_\infty \to 1$ configuration:*

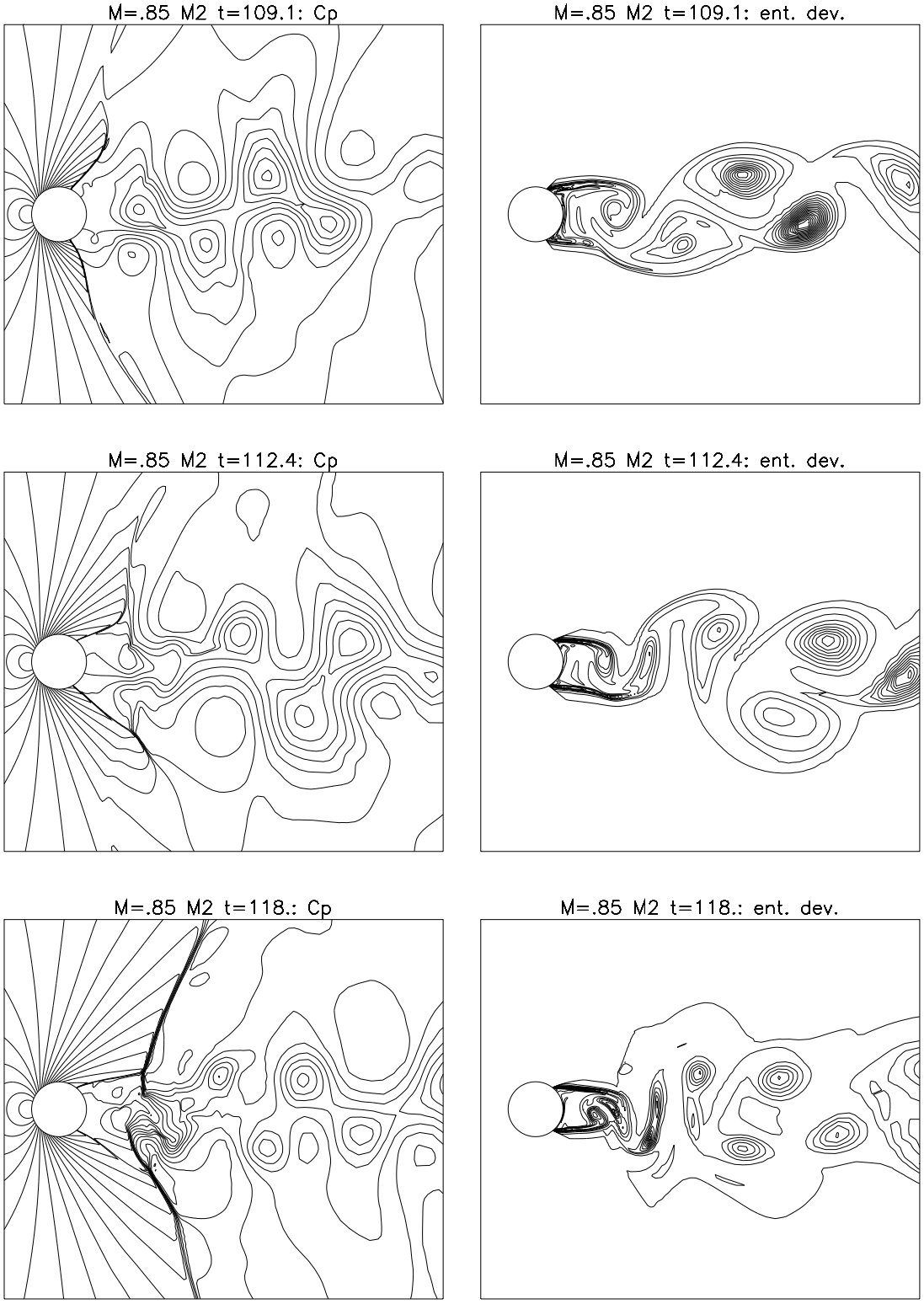

Figure 27: *$M_\infty = 0.85$, M2; pressure coeff. (left) and entropy deviation (right) contour lines. Towards the $M_\infty \to 1$ configuration:*

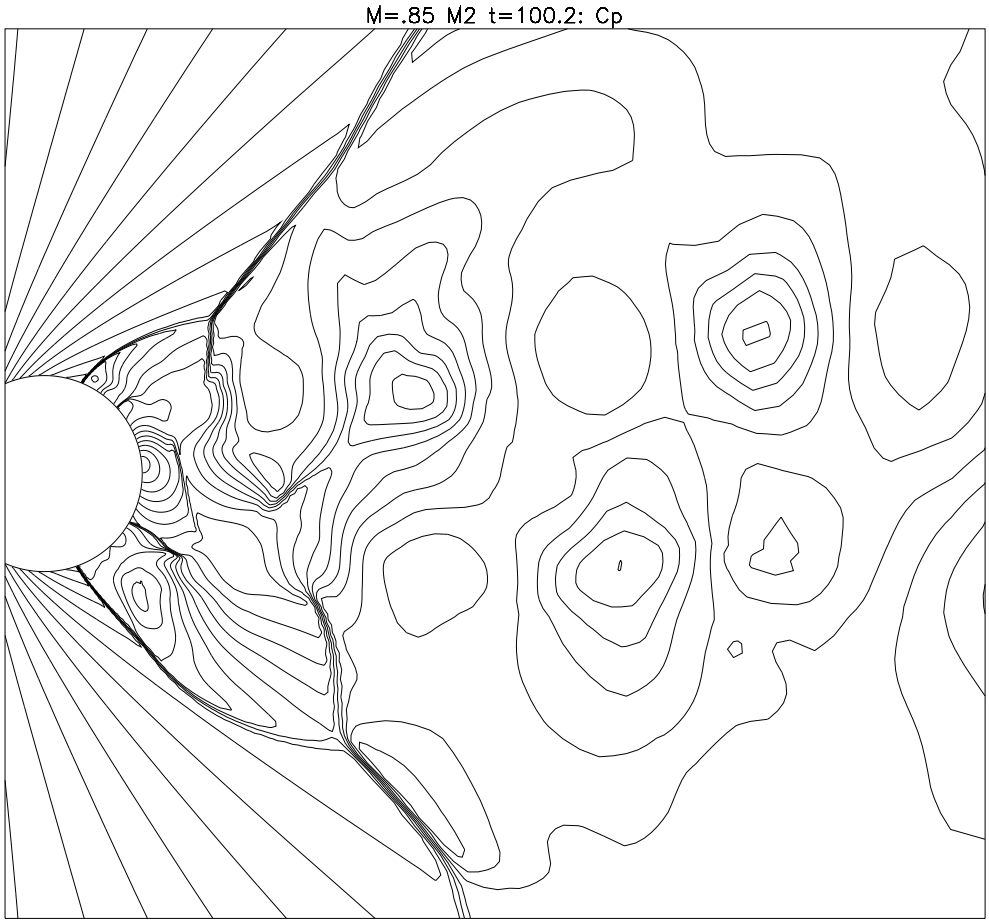

Figure 28: $M_\infty = 0.85$, *M2; pressure coefficient contour lines*

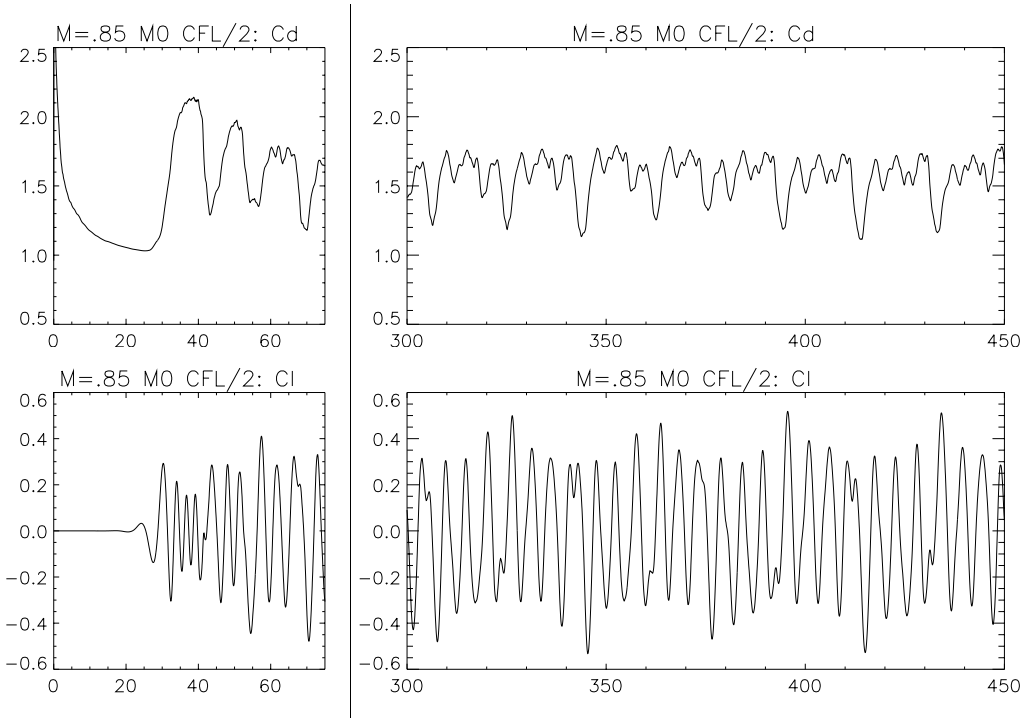

Figure 29: $M_\infty = 0.85$, *M0, CFL/2;* C_D *and* C_L *histories*

References

[1] M. D. Salas, *Recent developments in transonic Euler flow over a circular cylinder*, Mathematics and Computers in Simulation, Vol. XX-V, North-Holland, Amsterdam (1983).

[2] P. G. Buning and J. L. Steger, *Solution of the 2-dimensional Euler equations with generalized coordinate transformation using flux vector splitting*, AIAA Paper 82-0971 (1982).

[3] *GAMM workshop on Numerical Solution of the Euler Equations*, Notes on Numerical Fluid Mechanics, Vol. 26, Vieweg, 1989.

[4] M. Pandolfi and F. Larocca, *Transonic flow about a circular cylinder* Computers & Fluids, Vol. 17, No. 1, pp. 205-220, 1989.

[5] G. K. Batchelor, *An introduction to fluid dynamics* Cambridge University Press, 1967.

[6] R. J. LeVeque, *Numerical Methods for Conservation Laws* Birkhäuser, 1990.

[7] M. Pandolfi, *A contribution to the numerical prediction of unsteady flows*, AIAA Journal, Vol. 22, No. 5, May 1984, pp. 602-610.

[8] R. J. LeVeque, *Hyperbolic Conservation Laws and Numerical Methods*, Technical Report No. 90-3, March 1990, University of Washington

[9] N. Botta and J. Sesterhenn, *Deficiencies in the numerical computation of nozzle flow*, Research Report No. 92-05, May 1992.

[10] G. Moretti, *A technique for integrating two-dimensional Euler equations*, Computers & fluids, Vol. 15, No. 1, pp. 59-75, 1987.

[11] J. L. Thomas and M. D. Salas, *Far-field Boundary Conditions for Transonic Lifting Solutions to the Euler Equations*, AIAA Journal, Vol. 24, No. 7

[12] Di Mascio, Favini, Sabetta, G. Volpe, IX Congresso AIMETA, Pisa, 1990.

[13] A. Di Mascio, *Simulazione di flussi vorticosi mediante il modello di flusso compressibile non viscoso*, Tesi di Dottorato di Ricerca in Meccanica Applicata, Roma, Febbraio 1992.

Research Reports

No.	Authors	Title
92-15	N. Botta	Is the transonic flow around a cylinder always periodic?
92-14	K. Nipp, D. Stoffer	Invariant manifolds of numerical integration schemes applied to stiff systems of singular perturbation type - Part I: *RK*-methods
92-13	K. Nipp	Smooth attractive invariant manifolds of singularly perturbed ODE's
92-12	D. Mao	A Shock Tracking Technique Based on Conservation in One Space Dimension
92-11	K. Nipp, D. Stoffer	Attractive invariant manifolds for maps: Existence, smoothness and continuous dependence on the map
92-10	M. Fey, R. Jeltsch	A Simple Multidimensional Euler Scheme
92-09	M. Fey, R. Jeltsch	A New Multidimensional Euler Scheme
92-08	M. Fey, R. Jeltsch, P. Karmann	Numerical solution of a nozzle flow
92-07	M. Fey, R. Jeltsch, P. Karmann	Special aspects of reacting inviscid blunt body flow
92-06	M. Fey, R. Jeltsch, S. Müller	The influence of a source term, an example: chemically reacting hypersonic flow
92-05	N. Botta, J. Sesterhenn	Deficiencies in the numerical computation of nozzle flow
92-04	Ch. Lubich	Integration of stiff mechanical systems by Runge-Kutta methods
92-03	M. Fey, R. Jeltsch, S. Müller	Stagnation point analysis
92-02	C. W. Schulz-Rinne, J. P. Collins, H. M. Glaz	Numerical Solution of the Riemann Problem for Two-Dimensional Gas Dynamics
92-01	R. J. LeVeque, K. M. Shyue	Shock Tracking Based on High Resolution Wave Propagation Methods
91-10	M. Fey, R. Jeltsch	Influence of numerical diffusion in high temperature flow
91-09	R. J. LeVeque, R. Walder	Grid Alignment Effects and Rotated Methods for Computing Complex Flows in Astrophysics
91-08	Ch. Lubich, R. Schneider	Time discretization of parabolic boundary integral equations
91-07	M. Pirovino	On the Definition of Nonlinear Stability for Numerical Methods
91-06	Ch. Lubich, A. Ostermann	Runge-Kutta Methods for Parabolic Equations and Convolution Quadrature
91-05	C. W. Schulz-Rinne	Classification of the Riemann Problem for Two-Dimensional Gas Dynamics